

1 **Secondary magnetite in ancient zircon precludes analysis**
2 **of a Hadean geodynamo**

3

4 Fengzai Tang^a, Richard J. M. Taylor^{a1}, Josh F. Einsle^{a,e}, Cauê S. Borlina^b, Roger R. Fu^c, Benjamin P.
5 Weiss^b, Helen M. Williams^a, Wyn Williams^d, Lesleis Nagy^d, Paul Midgley^c, Eduardo A. Lima^b,
6 Elizabeth A. Bell^f, T Mark Harrison^f, Ellen W. Alexander^f, Richard J. Harrison^a

7

8 a. Department of Earth Sciences, University of Cambridge, Downing Street, Cambridge CB2 3EQ, UK
9 b. Department of Earth, Atmospheric, and Planetary Sciences, Massachusetts Institute of Technology, Cambridge, 02139, USA
10 c. Department of Earth and Planetary Sciences, Harvard University, Cambridge, Massachusetts 02138, USA
11 d. Geoscience Research Division, University of California San Diego, La Jolla, CA 92093, USA
12 e. Department of Materials Science and Metallurgy, University of Cambridge, UK
13 f. Department of Earth, Planetary, and Space Sciences, University of California, Los Angeles, California 90095, USA

14

15 1. corresponding author email: rjt79@cam.ac.uk

16

17 Keywords: Hadean | paleomagnetism | Jack Hills | zircon | correlative microscopy
18
19

20 **Abstract**

21 **Zircon crystals from the Jack Hills, Western Australia are one of the few surviving**
22 **mineralogical records of Earth's first 500 million years and have been proposed to contain a**
23 **paleomagnetic record of the Hadean geodynamo (1). A prerequisite for the preservation of**
24 **Hadean magnetization is the presence of primary magnetic inclusions within pristine igneous**
25 **zircon. To date no images of the magnetic recorders within ancient zircon have been presented.**
26 **Here we use high-resolution transmission electron microscopy to demonstrate that all observed**
27 **inclusions are secondary features formed via two distinct mechanisms. Magnetite is produced**
28 **via a pipe diffusion mechanism (2) whereby iron diffuses into radiation-damaged zircon along**
29 **the cores of dislocations and is precipitated inside nanopores and also during low-temperature**
30 **recrystallisation of radiation-damaged zircon in the presence of an aqueous fluid (3). Although**
31 **these magnetites can be recognised as secondary using transmission electron microscopy, they**
32 **otherwise occur in regions that are indistinguishable from pristine igneous zircon and carry**
33 **remanent magnetisation that post-dates the crystallisation age by at least several hundred**
34 **million years. Without microscopic evidence ruling out secondary magnetite, the paleomagnetic**
35 **case for a Hadean-Eoarchean geodynamo cannot yet be made.**

36
37 **Significance**

38 **The Earth's geodynamo is critical in protecting our atmosphere, and thus plays an important**
39 **role in the habitability of our planet. As such the Earth's magnetic field has likely played a**
40 **crucial role in the emergence of life around 4 billion years ago during the Hadean-Archean**
41 **Eons. However, we know little about the behaviour of the geodynamo during this critical**
42 **period. Recent efforts have focused on the magnetic signals harboured by Jack Hills zircon**
43 **crystals, the oldest terrestrial material. Here we show for the first time the magnetic carriers in**
44 **such grains. Our results demonstrate that while ancient zircon grains may contain ideal**
45 **magnetic recorders, they do not record the magnetic field strength at the time of zircon growth.**

46
47 The earliest paleomagnetic evidence for an active geodynamo comes from *c.* 3.45 billion year old
48 (Ga) rocks from the Barberton Greenstone Belt, and the Pilbara Craton (4-6). According to many core
49 formation models, the fields recorded by these rocks predate inner-core solidification, the process that
50 powers the present-day geodynamo through the release of light elements at the inner-core/outer-core
51 boundary. Prior to inner-core solidification, the geodynamo may have been powered by thermal
52 convection alone. Recent upward revision of core thermal conductivity (7-9) means that high heat
53 flux is needed to meet paleomagnetic constraints for a pure thermal dynamo. This leads to surprising
54 predictions of a very young inner core (<600 Ma) and initial core temperatures that were hot enough
55 to melt substantial portions of the lower mantle (10-12). As debate surrounding core thermal

56 conductivity, and implications for Earth's earliest magnetic fields continues (13), there is an ever-
57 increasing need to place robust paleomagnetic constraints on the early geodynamo.

58

59 The lack of data prior to 3.45 Ga leaves a gap of over a billion years in the paleomagnetic record.
60 Attempts to fill this gap have recently focused on the Jack Hills, Western Australia (1), where 2.65–
61 3.05 Ga metaconglomerates contain detrital zircon grains with U-Pb ages as old as 4.4 Ga (14).
62 Although zircon (ZrSiO_4) is not itself magnetic, zircon crystals contain inclusions of magnetic
63 minerals that make them potential targets for single-crystal paleomagnetic analysis (15). Tarduno et
64 al. (2015) (1) presented a single-crystal paleomagnetic study of Jack Hills detrital zircons, arguing
65 that zircons dated between 3.3 and 4.2 Ga contain primary thermoremanent magnetisation (TRM)
66 imparted by an active Hadean to Paleoproterozoic geodynamo. No microscopy images of primary
67 magnetic carriers within Jack Hills zircon have been presented to date. Rather, there is abundant
68 evidence for secondary magnetic sources on surfaces, along internal cracks, around multi-phase
69 micro-granite inclusions, and within metamict zones particularly for grains that have not been cleaned
70 with HCl (16). Constraining the source of magnetization – and demonstrating the lack of interference
71 by secondary remanence carriers (17) – is an essential step in confirming the robustness of Hadean
72 paleomagnetism. To this end, we performed the first direct study to determine the origin and setting of
73 ferromagnetic carriers in Jack Hills zircon using correlative magnetic measurements and electron
74 microscopy.

75

76 Zircon crystals were extracted from metaconglomerates of the Erawandoo Hill Hadean-zircon
77 discovery outcrop (18,19). We focus primarily on two grains (A and B) that are >3.9 Ga, and that
78 passed strict initial selection criteria for potential paleomagnetic targets: lack of evidence for
79 alteration from scanning electron microscopy (SEM) images, concordant U–Pb ages (Supplementary
80 Information E), and treatment with 6N HCl to remove Fe in cracks (16), and a stable natural remanent
81 magnetisation (NRM) component (Supplementary Information C). Three broadly defined textures are
82 seen in SEM images: (i) primary oscillatory zoning (ii) recrystallized zones with bright
83 cathodoluminescence (CL) (Grain B only) (iii) strongly radiation-damaged metamict zones
84 (individual oscillatory zones in Grain A, and the entire rim of Grain B). Specific areas (Fig. 1) were
85 targeted for scanning transmission electron microscopy (S/TEM) because of strong magnetic signals
86 observed in the zircon interior using quantum diamond microscopy (QDM) (20). TEM lamellae were
87 extracted from two grains targeting QDM signals within zones displaying primary oscillatory zoning
88 (Fig. 1a, e). Sample extraction was after thermal demagnetization experiments for Grains A and B,
89 but not for Grain C (Supplementary Information). Both heated and non-heated grains displayed
90 identical features. Magnetic regions are observed in some areas that display primary zoning and
91 recrystallized zones. Additional images are available in Supplementary Information A.

92

93 Grain A ($^{207}\text{Pb}^*/^{206}\text{Pb}^*$ age = 3979 Ma) clearly displays magnetic signals hosted by primary magmatic
94 zoning in SEM images (Fig. 1a-d). However, at the TEM scale, the lamella shows unequivocal
95 microstructural evidence of partial recovery from radiation damage with clearly observed porosity and
96 dislocations (Fig. 2a-c). This fluid-absent lattice recovery leads to the formation of nanoscale pores
97 that preferentially nucleate on dislocations, forming strings of pores linked by a common dislocation
98 line that crosscuts primary zonation (Fig. 2a). Dislocation cores concentrate non-structural elements
99 such as Fe, and provide fast pipe-diffusion pathways to deliver these elements from external sources
100 to an internal sink (2,21,22). Direct evidence of this mechanism is seen during the earliest stages of
101 infilling, where Fe accumulates at the intersection of the pore and the dislocation core (Fig. 2f). Pores
102 are frequently partially or fully filled with precipitate phases such as magnetite, ilmenite (FeTiO_3),
103 and crystalline ZrO_2 (potentially baddeleyite). The result is secondary, dislocation/pore-hosted,
104 nanoscale magnetite grains within zircon that appears unaltered at SEM scale. No magnetite was
105 found that does not lie on secondary microstructures, hence these observations demonstrate that all
106 the magnetite observed here post-dates primary zircon crystallization. A comprehensive set of images
107 of secondary magnetite and associated microstructures in Grain A can be found in Supplementary
108 Figure S2.

109

110 Grain B ($^{207}\text{Pb}^*/^{206}\text{Pb}^*$ age = 3973 Ma) shows similar features to A in primary oscillatory zoned areas,
111 along with an additional fluid-mediated recrystallisation zone also hosting magnetic signals.
112 Recrystallisation proceeds as a diffusion-reaction process in which hydrous species diffuse inwards
113 and catalyse structural recovery (3,23). We observe sinuous recrystallisation fronts with bright CL,
114 often closely associated with metamict areas that facilitate fluid ingress (Fig. 1j; Fig. S5a). These
115 recrystallized areas contain defect-rich crystalline zircon and crystallographically-oriented precipitates
116 of magnetite with elongated morphology due to preferential growth along intersecting dislocations
117 (Fig. S5f). These characteristics are typical of oxide inclusions precipitated from a silicate host by
118 heterogeneous nucleation on dislocations (24,25) and support a secondary origin for the magnetite in
119 the recrystallised zones. A comprehensive set of images of secondary magnetite and associated
120 microstructures in Grain B can be found in Supplementary Figures S4-6. Figure 3 demonstrates the
121 schematic progression of features seen in Grain B (Fig. 3a). The initial zircon grain shows oscillatory
122 zoning in CL, which reflects a variation in trace element content e.g U, and a high-U rim (Fig 3b).
123 Radiation damage slowly accumulates in the core, whilst the high-U rim becomes totally metamict.
124 Partial annealing of the core results in linked pore-dislocation networks, whilst the high-U rim
125 facilitates fluid ingress at a later stage, reorganizing the annealing microstructures (Fig 3c,f; Fig. S5a).
126 Magnetite growth in the core can only take place once this network of secondary features has
127 accumulated (Fig. 3d,f,g; Fig. S4a-d), and must therefore significantly post-date zircon crystallization.

128

129 Clear identification of the Fe-oxide as magnetite is the result of correlating the various datasets. Fe-
130 oxides observed chemically from STEM EDS were observed using Moiré fringe lattice interference
131 patterns between the zircon and oxide. The resultant Moiré fringe d-spacing (Fig 2d and
132 Supplementary Figure S11) defines the Fe-oxide as most likely magnetite, with a possibility of being
133 maghemite. However, the paleomagnetic data showing complete NRM demagnetization by 580°C
134 means it is only possible for the inclusions to be magnetite (Supplementary Figure S13). The
135 extraction of robust Hadean paleomagnetic signals from zircon single crystals relies on the following
136 assumptions about any given magnetic particle: i) iron oxide grains became trapped as primary
137 inclusions in igneous zircon; ii) inclusions within the zircon acquired a primary TRM during post-
138 crystallisation cooling and has not been subsequently reheated above the Curie temperature; iii)
139 armoured magnetic inclusions remained chemically and thermally unaltered by pre- and post-
140 depositional high-temperature metamorphic and low-temperature aqueous alteration/recrystallisation
141 events; iv) the high-temperature component of primary TRM can be separated from overlapping
142 sources of secondary magnetisation. If all these conditions are met, then the Jack Hills zircons have
143 the potential to constrain the properties of the Hadean geodynamo. If any one of these conditions is
144 violated, the case for primary magnetisation cannot be made.

145

146 We have observed two pathways for the formation of secondary single-domain magnetite in Jack
147 Hills zircon, circumventing criteria i and iii above. Formation of secondary magnetite in the presence
148 of a magnetic field will generate a chemical remanent magnetisation (CRM). An important property
149 of CRM is that its thermal unblocking temperature is not limited by the temperature of its acquisition,
150 but by the volume of the particles formed (26). Magnetite particles of sufficient size acquire CRM
151 with laboratory unblocking temperatures that overlap with the 550-585°C window attributed to
152 primary Hadean remanence (27). A representative (but not exhaustive) summary of magnetite
153 particles observed using TEM is given in Supplementary Table 1. Measurements of the length (L) and
154 width (W) of each particle were taken directly from the TEM images. Figure 4 compares the two-
155 dimensional, projected lengths and aspect ratios of the observed particles with the calculated
156 thresholds for superparamagnetic, single-domain and vortex behaviour in isolated magnetite particles
157 (28). The majority of observed particles are predicted to be single domain (Fig. 4a), with 40% of
158 grains having blocking temperatures $> 500^{\circ}\text{C}$ (Fig. 4b). Two of the largest particles observed are
159 predicted to lie above the threshold for single-vortex behaviour for non-interacting magnetite (28).
160 Micromagnetic simulations confirm that these particles adopt either single-domain or single-vortex
161 states at remanence, that both adopt vortex states during magnetization reversal, and that their
162 blocking temperatures are 570-575°C (Supplementary Information D). Single-vortex particles of a
163 similar size have been observed to retain their remanence all the way to the Curie temperature (29).

164 Thermal demagnetization of grain A demonstrates that 30-40% of its NRM is retained after heating to
165 550°C in zero field, and that the NRM is fully demagnetized by 580°C (Supplementary Information
166 C), confirming the presence of magnetite remanence carriers with high blocking temperatures. This
167 means that a putative primary Hadean TRM and secondary CRM would have overlapping blocking
168 spectra, making it difficult to discriminate primary and secondary remanence, violating criteria iv
169 above.

170

171 Given these observations of secondary ferromagnetism, recognising the presence of (or demonstrating
172 the lack of) secondary magnetite via high-resolution magnetic, compositional and mineralogical
173 analysis are now essential steps in the quest for Hadean paleomagnetism. Whilst most magnetite
174 particles formed through fluid-mediated recrystallization that we observed fall well within the stable
175 single-domain size range, their frequently low volumes yield blocking temperatures that mostly lie
176 outside the 550-585°C window used to isolate Hadean remanence. Therefore, CRM acquired via this
177 mechanism might be avoided through careful sample characterization and thermal demagnetisation to
178 550°C (27). However, the formation of secondary magnetite in crystalline zircon via the pipe-
179 diffusion mechanism cannot be recognized using CL imaging, is not associated with Pb loss, and
180 produces magnetite particles with sizes and aspect ratios spanning the stable single-domain to single-
181 vortex range, with blocking temperatures that fall within the 550-585°C window.

182

183 Evaluation of the TEM images in this study enables an estimate to be made of the volume expansion
184 of the crystal lattice due to radiation damage. Image analysis of the ratio of zircon to observed pore
185 spaces shows a volume expansion of approximately 0.7%, used as a proxy for lattice expansion,
186 which can be converted to the time taken to accumulate this damage based on the original actinide
187 content (30). Back-calculated U and Th concentrations give a lower estimate of *c.* 950 and *c.* 500
188 Myr, for grains A and B respectively, to produce the observed porosity (Supplementary Information B
189 provides more details). This means that the Fe source may be from fluid alteration within precursor
190 igneous rocks, but also allows for the source of Fe to be the Jack Hills sediment itself, consistent with
191 deep weathering estimates (31). This estimate provides an upper age limit for magnetite formation,
192 and is clearly significantly later than zircon crystallisation (Fig. 3).

193

194 The distinct possibility that the secondary Fe source predates sedimentation at 3.0 Ga is important, as
195 it negates the use of micro-conglomerate tests on the Jack Hills sediments as evidence for primary
196 magnetisation. The observed radiation damage in Jack Hills zircon is much lower than that expected
197 on the basis of their actinide content and age (32). Therefore, this pipe-diffusion mechanism is
198 expected to be widespread, a natural consequence of the build-up and subsequent recovery of

199 radiation damage that will affect all ancient zircon crystals. Therefore, unless primary magnetite can
200 be confirmed, the existence of a magnetic field during Eoarchean and Hadean remains an unknown.

201

202 **Methods**

203 1. SEM

204 An FEI Quanta 650 FEG-SEM (field emission gun- SEM) was use to collect both energy dispersive
205 spectroscopy (EDS) elemental maps (at 20 kV accelerating voltage), back scattered electron (BSE)
206 and cathodoluminescence (CL) micrographs (collected at 5 kV). The BSE and CL maps were
207 collected in parallel, while the EDS maps were collected subsequently. EDS maps were collected
208 using two Bruker 6l30 EDS detectors simultaneously to increase the overall counts and improve
209 throughput. For Grain C, each pixel's spectrum was denoised using a Python-based non-negative
210 matrix factorisation algorithm, background subtracted, and then peak integration performed on the
211 $Fe_{K\alpha}$ window of 6.0 – 6.7 keV (33,34).

212 2. TEM

213 The TEM specimen was site-precisely prepared from a zircon grain using a dual beam Focused Ion
214 Beam – Scanning Electron Microscope (FIB – SEM) FEI, now Thermo Fisher Scientific Inc., Helios
215 NanoLabTM (Hillsboro, Oregon, USA). An in-situ lift-out technique was applied to extract and
216 transfer the specimen onto a standard TEM molybdenum half grid, and a platinum bar was deposited
217 on the surfaces of target areas prior to FIB processing. The TEM lamella was made with the reduced
218 FIB voltages down to ~ 2-5 kV to minimize FIB-induced damage (35), and was cleaned for about 3-5
219 minutes in a plasma chamber before being loaded into the TEM microscope. The TEM study was
220 carried out using two microscopes: FEI Tecnai Osiris and FEI Titan³ (80-300 kV), and both were
221 dedicated to scanning TEM (STEM) operation. The Osiris microscope fitted with four silicon drift
222 detectors for energy dispersive X-ray spectrometry (EDS) analysis was used for STEM-HAADF
223 (high-angle annular dark field) and STEM-BF (bright field) imaging and fast STEM chemical
224 mapping operating at 200 kV. The Titan microscope had a probe forming corrector for spherical
225 aberration, allowing for high resolution imaging in STEM configuration at 300 kV. In order to obtain
226 optimum contrast for identifying nanometer-sized particles, the STEM imaging was typically taken at
227 the combination of the camera length between 80 - 250 mm and the screen currents of 0.05 - 0.3 nA,
228 whereas the STEM chemical mapping was performed at the screen currents larger than about 0.1 nA.

229 3. U-Pb Geochronology

230 Grains were pre-screened for ancient Pb isotope signatures on the CAMECA ims1270 ion
231 microprobe using a 15 nA O- primary beam and a mass resolution of 5000. This used more rapid
232 count times in order to analyse a large number of grains but at lower than normal precision. Oxygen
233 flooding to ca. 1×10^{-5} torr was used to enhance Pb ionization. Following a 2-minute presputter to
234 clean the zircon surface, Pb isotopes were counted for 30 seconds in monocollection mode. During a
235 later session, U-Pb ages were measured under the more typical instrumental conditions and count

236 times, using the AS3 zircon standard³⁶ for Pb/U relative sensitivity factor calibration. More details on
237 the U-Pb method can be found in Quidelleur, et al. (37).

238 4. QDM

239 We use the quantum diamond microscope (QDM) at the Harvard Paleomagnetism Laboratory
240 to obtain high-resolution magnetic field maps of zircon grains A and B (Fig. 1C,G). Both grains are
241 first subjected to a 0.25 T isothermal remanent magnetization (IRM) oriented out of the imaging
242 plane. The polished surface of the zircons is then placed in contact with the sensing diamond, which
243 has nitrogen-vacancy (N-V) centers implanted uniformly in a 4 μm layer. We then optically excite
244 the (N-V) centers with a 500 mW 532 nm wavelength laser and image the fluorescence at a spatial
245 resolution of 1.17 μm per pixel. To maximize the signal-to-noise ratios, we perform the experiments
246 in projective magnetic microscopy (PMM) mode (21) that directly measures the magnetic field
247 projection in the [111] direction of the diamond lattice. This protocol involves two measurements
248 taken under bias fields of 900 μT oriented in opposing directions parallel to the [111] axis. The two
249 maps are then summed to isolate the ferromagnetic component. The reversal accuracy of the bias
250 field is 1 part in 1500, resulting in a residual bias field of 600 nT, which is then subtracted from the
251 summed map. The residual bias field in the final map is therefore at least 10^3 smaller than the zircon
252 signals and can be neglected. We then convert these projected magnetic field values to the magnetic
253 field perpendicular to the measurement plane using spectral domain algorithm (38).

254 5. Laser ablation

255 U and Th measurements were made for the zircon grains alongside the TEM locations in
256 order to calculate radiation damage times. Analyses were carried out using an ESI UP193UC laser
257 system coupled to a Perkin Elmer Nexion 350D Inductively Coupled Plasma Mass Spectrometer (LA-
258 ICP-MS) in the Department of Earth Sciences at the University of Cambridge. The LA-ICP-MS data
259 acquisition settings were 1 sweep per reading, 80 readings, 1 replicate, and total data acquisition
260 lasted 50 seconds (approximately 1 data point for each element per second). The instrument was set
261 up for background data followed by ablation for 20 seconds, at a rep rate of 10 Hz and power on the
262 sample of $\sim 3 \text{ Jcm}^2$. Data was processed using Iolite software with the trace element DRS (39), with
263 concentrations calibrated against KLDF standard zircon (Curtin University internal standard; U 507
264 ppm Th 74 ppm) and 91500 (40). With NIST glasses SRM 610 and 612 (41) run to monitor instrument
265 stability. U and Th concentrations were calculated for the crystallization ages of the grains.

266

267

268 **Acknowledgements**

269 The authors would like to thank two anonymous reviewers for their constructive comments that
270 greatly improved the manuscript. The research leading to these results has received funding from the
271 European Research Council under the European Union's Seventh Framework Programme (FP/2007-

272 2013) / ERC Grant Agreement No. 320750, NERC grant NE/P002498/1, National Science
273 Foundation grant EAR1647504, and Thomas F. Peterson, Jr. The UCLA ion microprobe facility is
274 partly supported by a grant from the Instrumentation and Facilities Program, Division of Earth
275 Sciences, NSF (1339051)

276 .

277 **Competing interests**

278 The authors declare no competing interests

279

280 **Author Contributions**

281 FT - TEM sample preparation and analysis. RJMT - Manuscript text and figure preparation, SEM
282 analysis of zircon, interpretation of zircon textures and microstructure. JFE - SEM analysis of zircon.
283 CSB EAL - Paleomagnetic measurements of zircon grains and data interpretation. RRF - QDM
284 measurements of zircon grains. BPW - Interpretation of QDM and paleomagnetic measurements.
285 HMW - Interpretation of Fe-oxide morphologies, grant CoI. WW LN - Micromagnetic modeling and
286 interpretation of results. PM - Interpretation of micro/nano structures. EAB TMH EWA - U-Pb
287 measurements, Li zoning analysis, fieldwork. RJH - Grant PI, manuscript preparation, interpretation
288 of TEM, QDM and micromagnetic modelling results. All Authors contributed to the editing of the
289 submitted manuscript

290

291 **References**

- 292 1. Tarduno, J. A., Cottrell, R. D., Davis, W. J., Nimmo, F. & Bono, R. K. A. (2015) Hadean to
293 Paleoproterozoic geodynamo recorded by single zircon crystals. *Science* **349**, 521-524,
294 doi:10.1126/science.aaa9114
- 295 2. Piazzolo, S. *et al.* (2016) Deformation-induced trace element redistribution in zircon revealed using
296 atom probe tomography. *Nature Communications* **7**, 1, 91-107. 10490, doi:10.1038/ncomms10490
297 <https://www.nature.com/articles/ncomms10490> - supplementary-information (2016)
- 298 3. Geisler, T., Schaltegger, U. & Tomaschek, F. (2007). Re-equilibration of zircon in aqueous fluids
299 and melts. *Elements* **3**, 43-50
- 300 4. Tarduno, J. A. *et al.* (2010) Geodynamo, solar wind, and magnetopause 3.4 to 3.45 billion years
301 ago. *Science* **327**, 1238-1240, doi:10.1126/science.1183445.
- 302 5. Biggin, A. J. *et al.* (2011) Palaeomagnetism of Archean rocks of the Onverwacht Group, Barberton
303 Greenstone Belt (southern Africa): Evidence for a stable and potentially reversing geomagnetic field
304 at ca. 3.5Ga. *Earth and Planetary Science Letters* **302**, 314-328, doi:10.1016/j.epsl.2010.12.024.
- 305 6. McElhinny, M. & Senanayake, W. (1980) Paleomagnetic evidence for the existence of the
306 geomagnetic field 3.5 Ga ago. *Journal of Geophysical Research: Solid Earth* **85**, 3523-3528.
- 307 7. Gomi, H. *et al.* (2013) The high conductivity of iron and thermal evolution of the Earth's core.
308 *Physics of the Earth and Planetary Interiors* **224**, 88-103, doi:10.1016/j.pepi.2013.07.010.
- 309 8. Pozzo, M., Davies, C., Gubbins, D. & Alfè, D. (2013) Transport properties for liquid silicon-oxygen-
310 iron mixtures at Earth's core conditions. *Physical Review B* **87**, 014110.
- 311 9. Ohta, K., Kuwayama, Y., Hirose, K., Shimizu, K. & Ohishi, Y. (2016) Experimental determination of
312 the electrical resistivity of iron at Earth's core conditions. *Nature* **534**, 95.
- 313 10. Davies, C., Pozzo, M., Gubbins, D. & Alfè, D. (2015) Constraints from material properties on the
314 dynamics and evolution of Earth's core. *Nature Geoscience* **8**, 678, doi:10.1038/ngeo2492

315 <https://www.nature.com/articles/ngeo2492> - supplementary-information.

316 11. O'Rourke, J. G., Korenaga, J. & Stevenson, D. J. (2017) Thermal evolution of Earth with
317 magnesium precipitation in the core. *Earth and Planetary Science Letters* **458**, 263-272.

318 12. Badro, J., Siebert, J. & Nimmo, F. (2016) An early geodynamo driven by exsolution of mantle
319 components from Earth's core. *Nature* **536**, 326.

320 13. Konôpková, Z., McWilliams, R. S., Gómez-Pérez, N. & Goncharov, A. F. (2016) Direct
321 measurement of thermal conductivity in solid iron at planetary core conditions. *Nature* **534**, 99,
322 doi:10.1038/nature18009.

323 14. Valley, J. W. *et al.* (2014) Hadean age for a post-magma-ocean zircon confirmed by atom-probe
324 tomography. *Nature Geoscience* **7**, 219-223, doi:10.1038/ngeo2075.

325 15. Fu, R. R. *et al.* (2017) Evaluating the paleomagnetic potential of single zircon crystals using the
326 Bishop Tuff. *Earth and Planetary Science Letters* **458**, 1-13, doi:10.1016/j.epsl.2016.09.038.

327 16. Weiss, B. P. *et al.* (2018) Secondary magnetic inclusions in detrital zircons from the Jack Hills,
328 Western Australia, and implications for the origin of the geodynamo. *Geology* **5**, 427-430.

329 17. Weiss, B. P. *et al.* (2015) Pervasive remagnetization of detrital zircon host rocks in the Jack Hills,
330 Western Australia and implications for records of the early geodynamo. *Earth and Planetary Science*
331 *Letters* **430**, 115-128, doi:10.1016/j.epsl.2015.07.067.

332 18. Maas, R., Kinny, P. D., Williams, I. S., Froude, D. O. & Compston, W. (1992) The Earth's oldest
333 known crust: A geochronological and geochemical study of 3900-4200 Ma old detrital zircons from
334 Mt. Narryer and Jack Hills, Western Australia. *Geochimica et Cosmochimica Acta* **56**, 1281-1300.

335 19. Wilde, S. A., Valley, J. W., Peck, W. H. & Graham, C. M. (2001) Evidence from detrital zircons for
336 the existence of continental crust and oceans on the Earth 4.4 Gyr ago. *Nature* **409**, 175-178,
337 doi:10.1038/35051550.

338 20. Glenn, D. R. *et al.* (2017) Micrometer-scale magnetic imaging of geological samples using a
339 quantum diamond microscope. *Geochemistry, Geophysics, Geosystems* **18**, 8, 3254-3267.

340 21. Timms, N. E., Reddy, S. M., Gerald, J. D. F., Green, L. & Muhling, J. R. (2012) Inclusion-localised
341 crystal-plasticity, dynamic porosity, and fast-diffusion pathway generation in zircon. *Journal of*
342 *Structural Geology* **35**, 78-89.

343 22. White, L. F. *et al.* (2017) Atomic-scale age resolution of planetary events. *Nature*
344 *Communications* **8**, 1-6.

345 23. Geisler, T., Pidgeon, R. T., Kurtz, R., van Bronswijk, W. & Schleicher, H. (2003) Experimental
346 hydrothermal alteration of partially metamict zircon. *American Mineralogist* **88**, 1496-1513.

347 24. Lappe, S. C. L. L. *et al.* (2011) Mineral magnetism of dusty olivine: A credible recorder of pre-
348 accretionary remanence. *Geochemistry, Geophysics, Geosystems* **12**, 12, 1-20.
349 doi:10.1029/2011GC003811.

350 25. Einsle, J. F. *et al.* (2016) Multi-scale three-dimensional characterization of iron particles in dusty
351 olivine: Implications for paleomagnetism of chondritic meteorites. *American Mineralogist* **101**, 2070-
352 2084, doi:10.2138/am-2016-5738CCBY.

353 26. McClelland-Brown, E. (1982) Discrimination of TRM and CRM by blocking-temperature spectrum
354 analysis. *Physics of the Earth and Planetary Interiors* **30**, 405-414.

355 27. Tarduno, J. A. & Cottrell, R. D. (2013) Signals from the ancient geodynamo: A paleomagnetic field
356 test on the Jack Hills metaconglomerate. *Earth and Planetary Science Letters* **367**, 123-132,
357 doi:10.1016/j.epsl.2013.02.008.

358 28. Muxworthy, A. R. & Williams, W. (2008) Critical superparamagnetic/single-domain grain sizes in
359 interacting magnetite particles: implications for magnetosome crystals. *Journal of the Royal Society*
360 *Interface*, rsif. 2008.0462.

361 29. Almeida, T. P. *et al.* (2016) Direct visualization of the thermomagnetic behavior of pseudo-single-
362 domain magnetite particles. *Science advances* **2**, e1501801.

363 30. Murakami, T., Chakoumakos, B. C., Ewing, R. C., Lumpkin, G. R. & Weber, W. J. (1991) Alpha-
364 decay event damage in zircon. *American Mineralogist;(United States)* **76**.

- 365 31. Pidgeon, R.T., Nemchin, A.A., and Whitehouse, M.J., (2017) The effect of weathering on U–Th–
366 Pb and oxygen isotope systems of ancient zircons from the Jack Hills, Western Australia: *Geochimica*
367 *et Cosmochimica Acta*, v. 197, p. 142–166.
- 368 32. Pidgeon, R. Zircon radiation damage ages. *Chemical Geology* **367**, 13-22 (2014).
- 369 33. Lee, D. D. & Seung, H. S. (1999) Learning the parts of objects by non-negative matrix
370 factorization. *Nature* **401**, 788.
- 371 34. Hyperspy. doi:hyperspy/hyperspy: HyperSpy 1.1.2. (2017). doi:10.5281/zenodo.240660 (2017).
- 372 35. Tang, F. *et al.* (2018) Nanoscale structural and chemical analysis of F-implanted enhancement-
373 mode InAlN/GaN heterostructure field effect transistors. *Journal of Applied Physics* **123**, 024902.
- 374 36. Paces, J. B. & Miller, J. D. (1993) Precise U-Pb ages of Duluth complex and related mafic
375 intrusions, northeastern Minnesota: Geochronological insights to physical, petrogenetic,
376 paleomagnetic, and tectonomagmatic processes associated with the 1.1 Ga midcontinent rift
377 system. *Journal of Geophysical Research: Solid Earth* **98**, 13997-14013.
- 378 37. Quidelleur, X. *et al.* (1997) Thermal evolution and slip history of the Renbu Zedong Thrust,
379 southeastern Tibet. *Journal of Geophysical Research: Solid Earth* **102**, 2659-2679.
- 380 38. Lima, E. A. & Weiss, B. P. (2009) Obtaining vector magnetic field maps from single-component
381 measurements of geological samples. *Journal of Geophysical Research: Solid Earth* **114**,
382 doi:10.1029/2008JB006006.
- 383 39. Paton, C., Hellstrom, J., Paul, B., Woodhead, J. & Hergt, J. (2011) Lolite: Freeware for the
384 visualisation and processing of mass spectrometric data. *Journal of Analytical Atomic Spectrometry*
385 **26**, 2508-2518.
- 386 40. Wiedenbeck, M. *et al.* (2004) Further characterisation of the 91500 zircon crystal. *Geostandards*
387 *and Geoanalytical Research* **28**, 9-39.
- 388 41. Pearce, N. J. G. *et al.* (1997) A compilation of new and published major and trace element data
389 for NIST SRM 610 and NIST SRM 612 glass reference materials. *Geostandards Newsletter* **21**, 115-
390 144.
- 391
- 392

393 **Figure Captions**

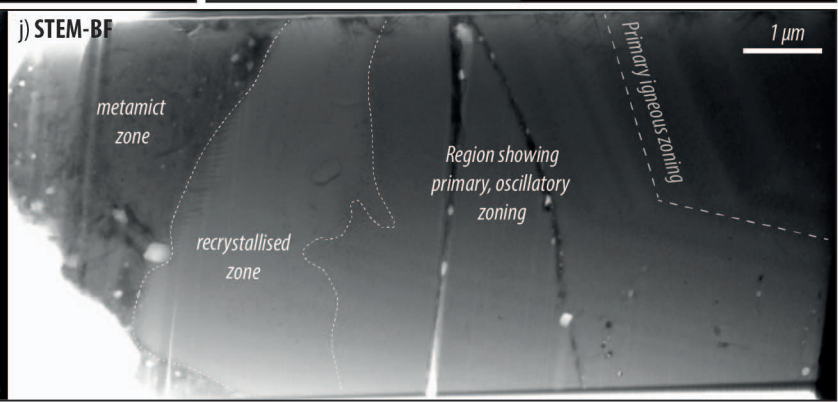
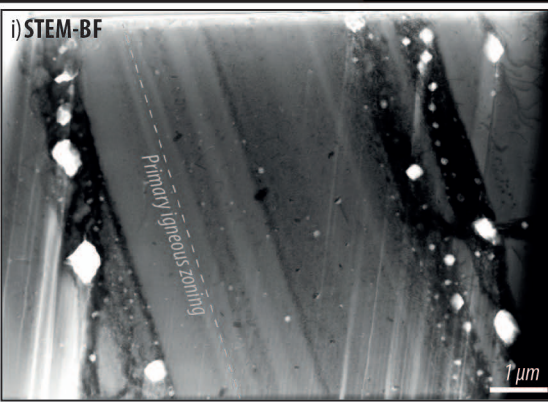
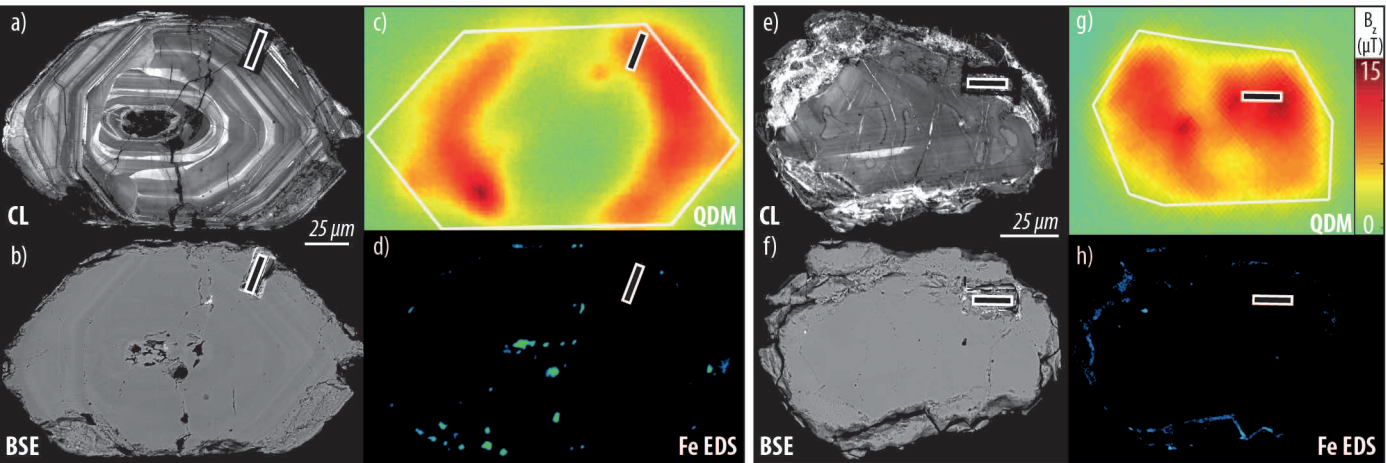
394
395 Figure 1. Summary of SEM (a-h) and TEM (i-j) images of Jack Hills zircon grains A and B in this
396 study. White outline rectangles mark original location of TEM lamellae. SEM – Grain A: a) CL image
397 showing primary igneous zoning; b) BSE image; c) QDM magnetic anomaly map; d) Compositional
398 map of Fe intensity. Grain B: e) CL image showing primary igneous zoning; f) BSE image; g) QDM
399 magnetic anomaly map; h) Compositional map of Fe intensity. Note that e) and f) were taken after a
400 final polish, so that the TEM foil location appears less central than in g), which was taken prior to
401 final polish. i) TEM lamella showing primary zoning and associated secondary inclusions in grain A;
402 j) TEM lamella showing primary zoning (RHS) and secondary inclusions in grain B. Metamict areas,
403 and a fluid-assisted recrystallization zone appear on the LHS. Colour scale shown in g) also applies to
404 c).

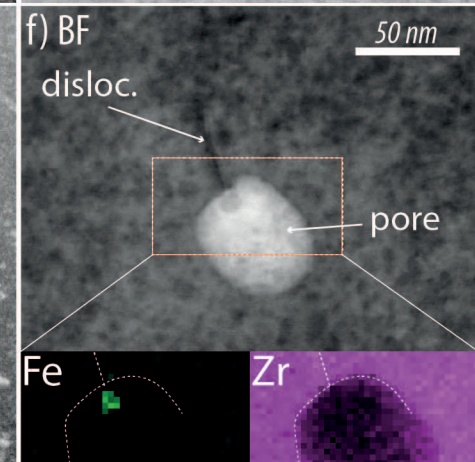
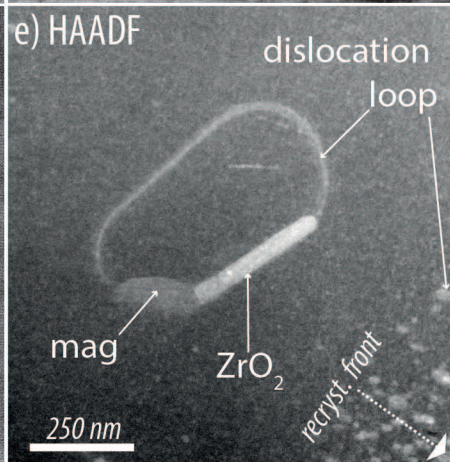
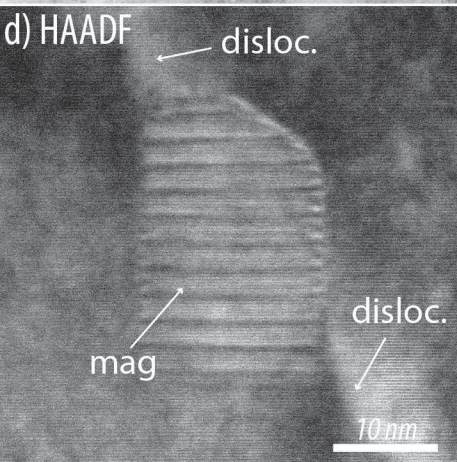
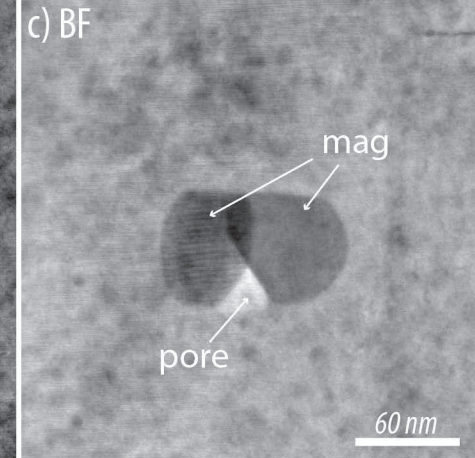
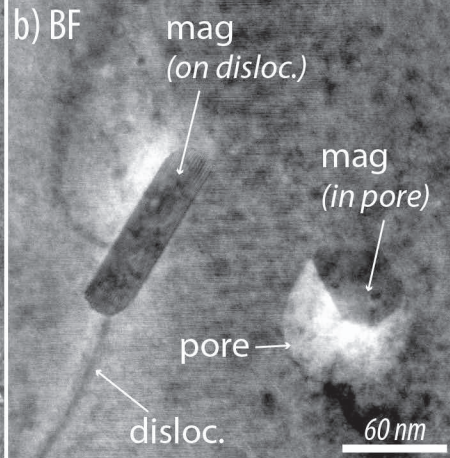
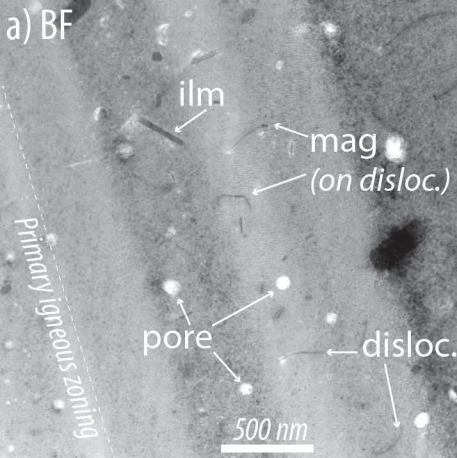
405
406 Figure 2. HR-STEM images of nanoscale features and inclusions in this study. BF = bright field,
407 HAADF = high angle annular dark field. Background matrix is zircon. a) Broad view of primary
408 zoning with secondary features related to recovery of radiation damage. b) Secondary magnetite
409 grains along dislocations and filling pore spaces. c) Multiple magnetite crystals in single pore. d)
410 Example of Moiré fringe data used to identify magnetite. e) Dislocation loop with magnetite and ZrO₂
411 near recrystallization front (see Fig. 3e). f) Intersection of dislocation and pore demonstrating pipe
412 diffusion of secondary Fe into pore spaces; insets show Fe and Zr EDS maps. Mineral abbrev. ilm –
413 ilmenite; mag – magnetite;. Images a-d from Grain A; image e from Grain B; images d and f are from
414 additional grain C (see Supplementary Information A). Images a-c Grain A, Image e Grain B, Images
415 d & f Grain C (See Supplementary Information A).

416
417 Figure 3. Summary diagram showing order of events forming secondary inclusions in Brain B. a)
418 TEM BF image of lamella. b) Schematic of zoning in zircon. Oscillatory zoning with variable U
419 content (light = low U) accumulating radiation damage at different rates. High U rim area
420 accumulates damage most rapidly. c) Fluid-mediated recrystallisation and fluid-absent recovery
421 process occur 100s Myr after grain formation. d) Fe infiltrates dislocation-pore network forming
422 magnetite. e-g) Close up of processes inset areas in panels c and d. Features shown in f and g are clear
423 in images from Supplementary S4 a-d.

424
425 Figure 4. Magnetic information on secondary magnetite particles observed in Jack Hills zircon. a)
426 Length (L) vs aspect ratio (W/L) for magnetite particles observed using TEM (see Supplementary
427 Table 1). Boundaries between superparamagnetic, single-domain and vortex states are based on
428 micromagnetic simulations of non-interacting magnetite (Muxworthy and Williams, 2008). b)
429 Histogram of calculated blocking temperatures (50 °C bin width), excluding SP particles. Blocking

430 temperatures were calculated for laboratory observation times (taken to be $t_{\text{obs}} = 100$ sec). A
431 significant number of the particles observed have $T_{\text{B}} > 500$ °C, consistent with the rapid loss of NRM
432 observed using SQUID magnetometry (Supplementary Figure 13).

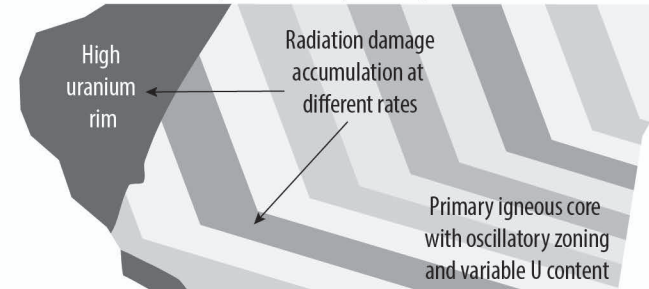




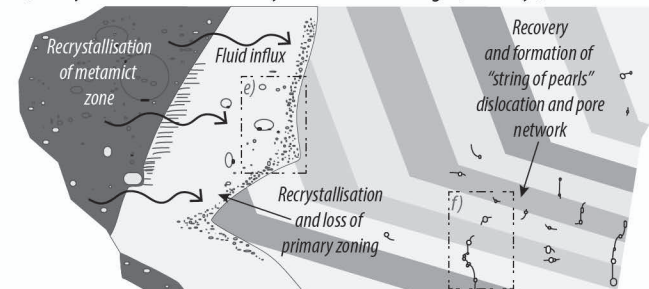
a) TEM foil image from grain B showing multiple textures



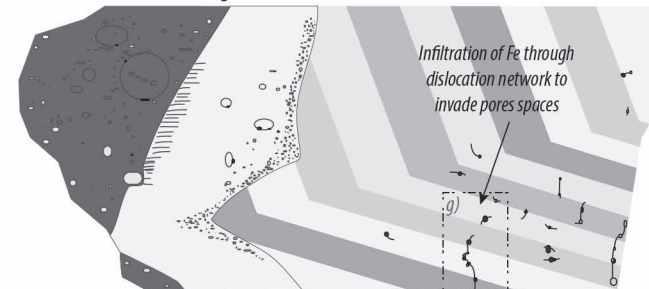
b) Schematic of TEM foil prior to recovery and recrystallisation



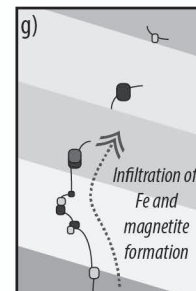
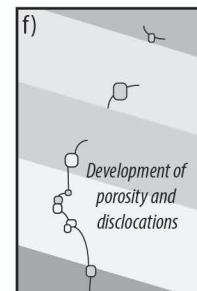
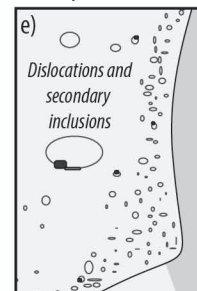
c) Recrystallisation and recovery of radiation damage (100's Myr)

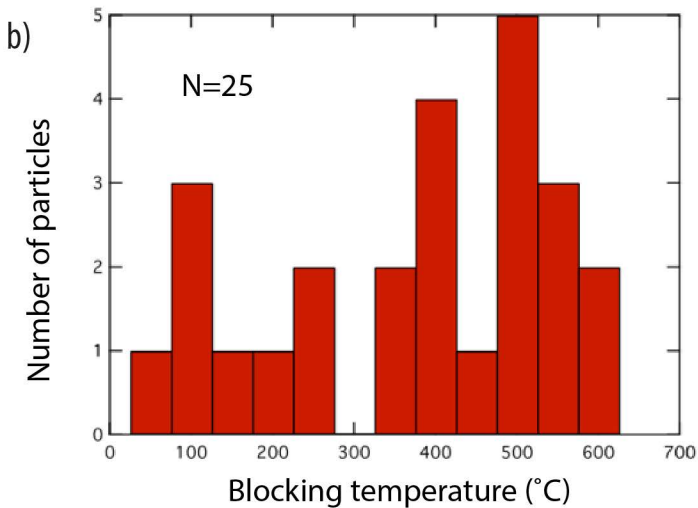
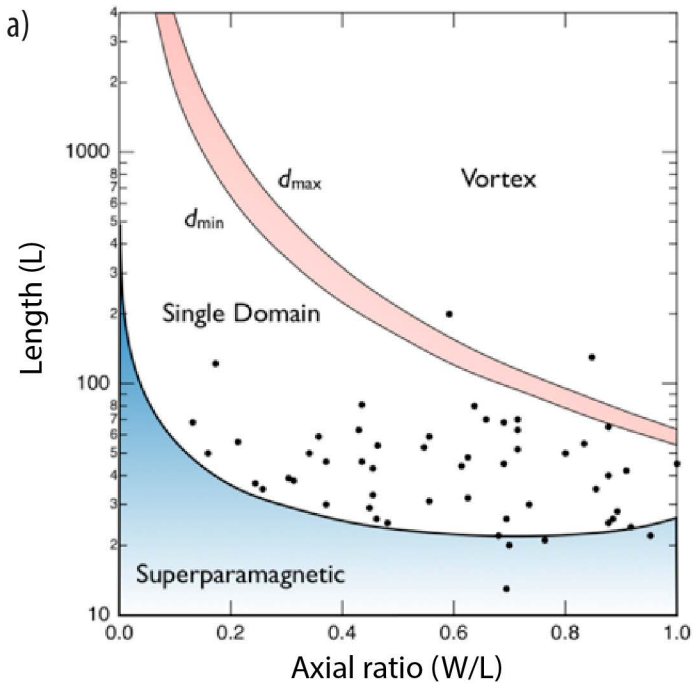


d) Infiltration of Fe through dislocation network



Close up of textures in schematic





Secondary magnetite in ancient zircon precludes analysis of a Hadean geodynamo

Fengzai Tang^a, Richard J. M. Taylor^{a1}, Josh F. Einsle^{a,e}, Cauê S. Borlina^b, Roger R. Fu^c, Benjamin P. Weiss^b, Helen M. Williams^a, Wyn Williams^d, Lesleis Nagy^d, Paul Midgley^e, Eduardo A. Lima^b, Elizabeth A. Bell^f, T Mark Harrison^f, Ellen Alexander^f, Richard J. Harrison^a

1. corresponding author email: rjt79@cam.ac.uk

This PDF file includes:

Supplementary sections A-E

A) Additional TEM images

- Grain A : S1 – S2
- Grain B : S3 – S6
- Grain C : S7 – S11

B) Radiation damage model

C) Paleomagnetic data

D) Micromagnetic modelling

E) Uranium-Lead dating

Figs. S1 to S14

Legends for movies S15 to S16

References for SI reference citations

Table S1

Other supplementary materials for this manuscript include the following:

Movies S15 to S16

Supplementary information A – Additional grain information and images

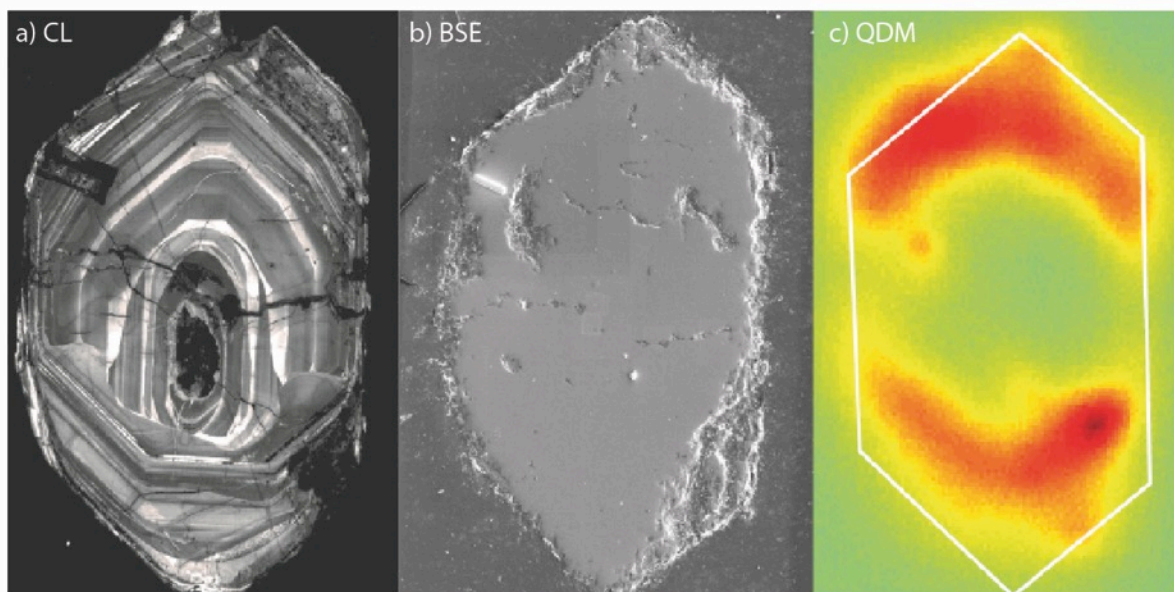
Original grain names in research project:

Grain A – 080211_h30

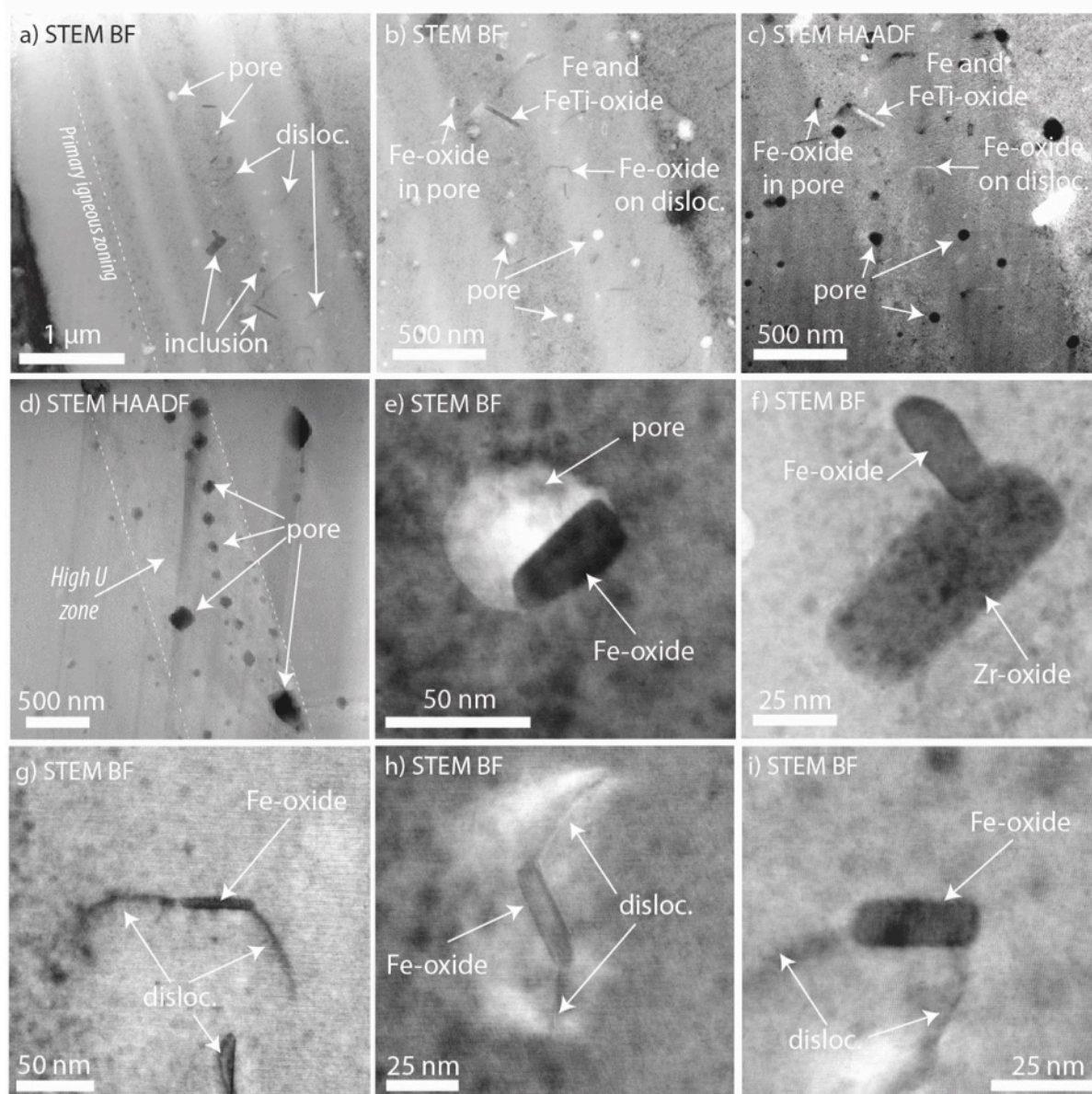
Grain B – 071320_h02

Grain C – D175M-B2-1-4

Grain A



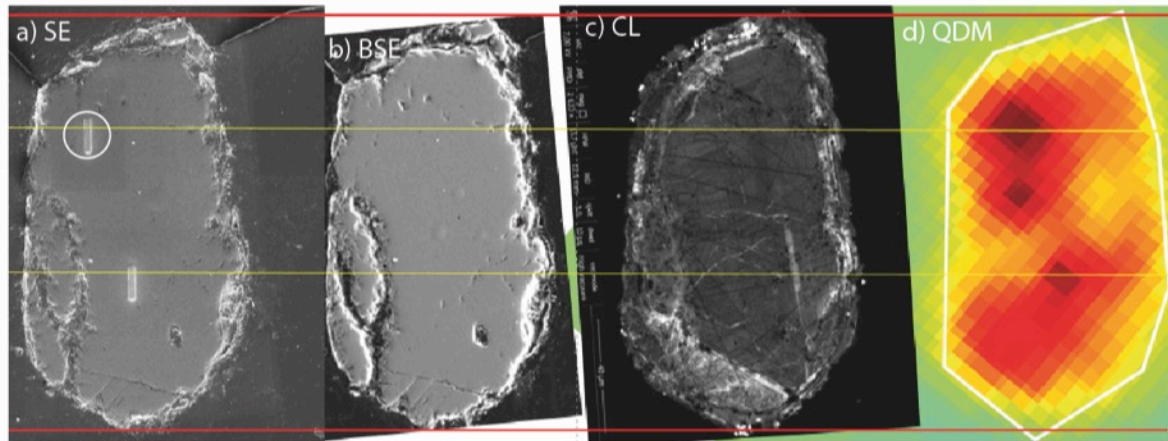
Supplementary Figure S1. SEM and magnetic images of Grain A. This zircon at first glance may appear to be a good example of a potential paleomagnetic target for the early Earth. It shows almost uniform, continuous oscillatory zoning indicative of primary igneous growth. The CL image does not show any significant recrystallization zones, or metamorphic overgrowths. Other than a few late cracks, the BSE image is very flat, suggesting a good grain quality. The QDM image highlights magnetic portions of the grain that are spatially associated with the primary zoning, suggesting the incorporation of primary magnetite during crystallisation. However, a TEM foil extracted from one such zone (top left in images) found that all magnetite is associated with secondary recrystallization features.



Supplementary Figure S2. STEM images of TEM foil extracted from Grain A. a) Overview BF image, highlighting the contrast between primary oscillatory zones, secondary microstructures, pores and inclusions. b-c) BF and HAADF image of the same area, demonstrating the contrast of various features used to identify microstructures and inclusions. Images are dominated by the zircon matrix in mid grey, showing primary zoning. The BF image shows low density features such as pore spaces as bright areas, whilst high-density inclusions such as magnetite, ZrO_2 and ilmenite appear slightly darker. HAADF image shows opposing greyscale with density, and highlights some features more clearly. d) Image showing one of the more radiation-damaged (higher U) primary zones (see main text Figure 1i). Initially these areas were investigated as potential sources of magnetism, but they were found to be dominated by empty pore space and very few inclusions compared to other zones. e) Example of Fe-oxide grain partially filling a pore space that was generated through recovery of radiation damage. f) Example of Fe-oxide grain associated with other secondary inclusions, in this

case ZrO_2 . g-i) Multiple examples of typical magnetic sources observed in recovered, oscillatory zoned area. Fe-oxide particles are elongate and associated with secondary dislocation microstructures.

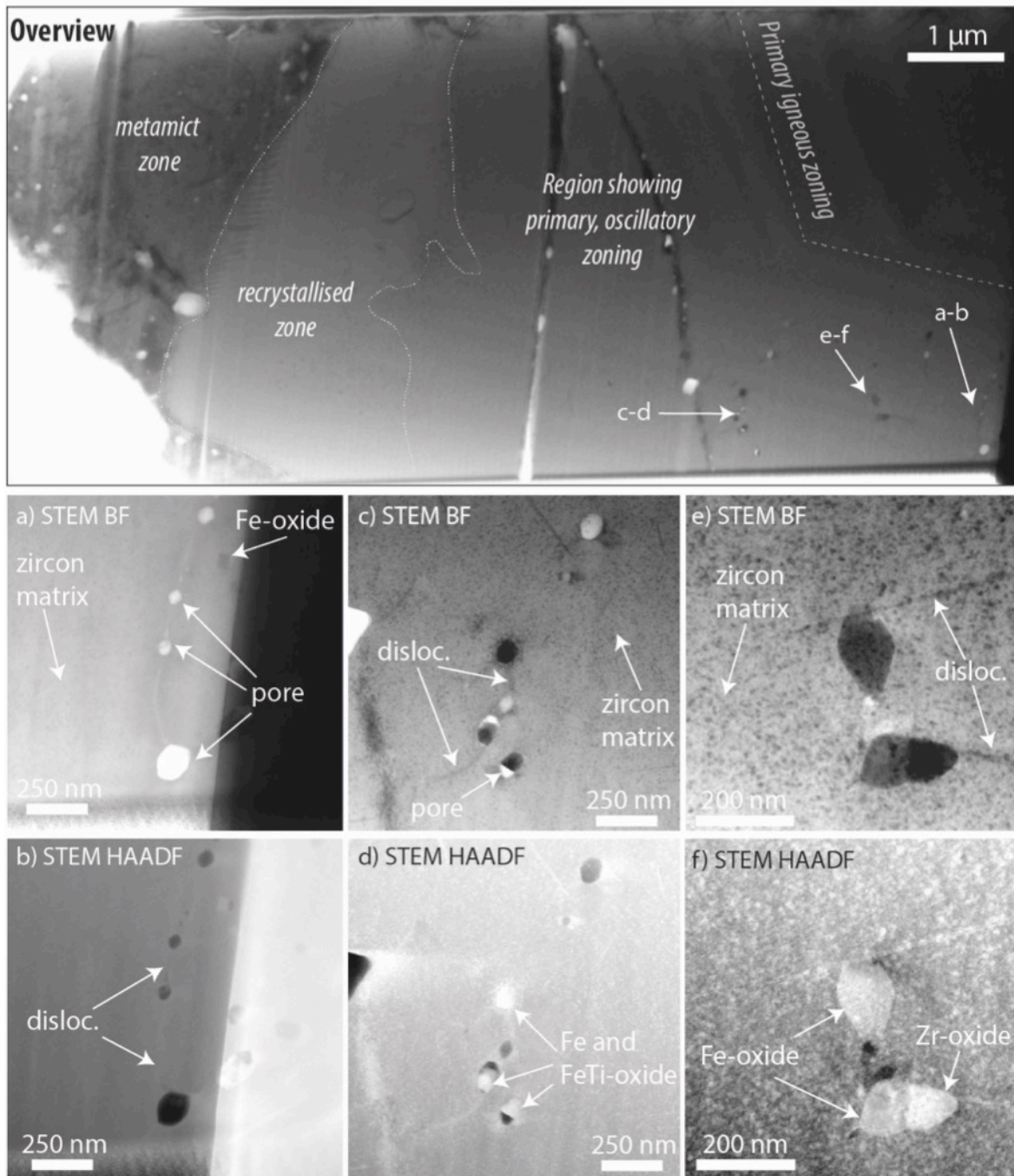
Grain B



Supplementary Figure S3. SEM and magnetic images of Grain B used for targeting prior to extraction of TEM foil. Left to right: SE, BSE, CL, QDM. QDM images shows locations of target areas of interest prior to the TEM study. White circle shows location of TEM extraction site (second site near centre of grain was not studied). This supplementary figure set shows the true location of the TEM foil with respect to targeting images, and can be seen to be predominantly within the core (oscillatory zoned region) of the grain. However, the polish at this stage was not suitable for CL imaging. The main manuscript figures give the impression the foil was extracted more in the metamict rim; however, this was after an additional polish to show the internal features in CL.

Grain B is made up of 3 distinct zones: an oscillatory zoned core, representing igneous crystallisation and recovered radiation damage; a highly radiation-damaged zone around the edge of the grain; and a zone in between which shows evidence of fluid assisted recrystallization. Zones showing primary zoning and recrystallization textures show nanoscale magnetite particles responsible for secondary magnetic signals. The TEM foil for this grain traverses all three zones showing multiple examples of Fe-oxide inclusions. Late cracks are seen through the core, which may accommodate a number of macroscale secondary features, and are not the focus of this study (see Weiss et al., 2018). Additional images to compliment the main text are shown below.

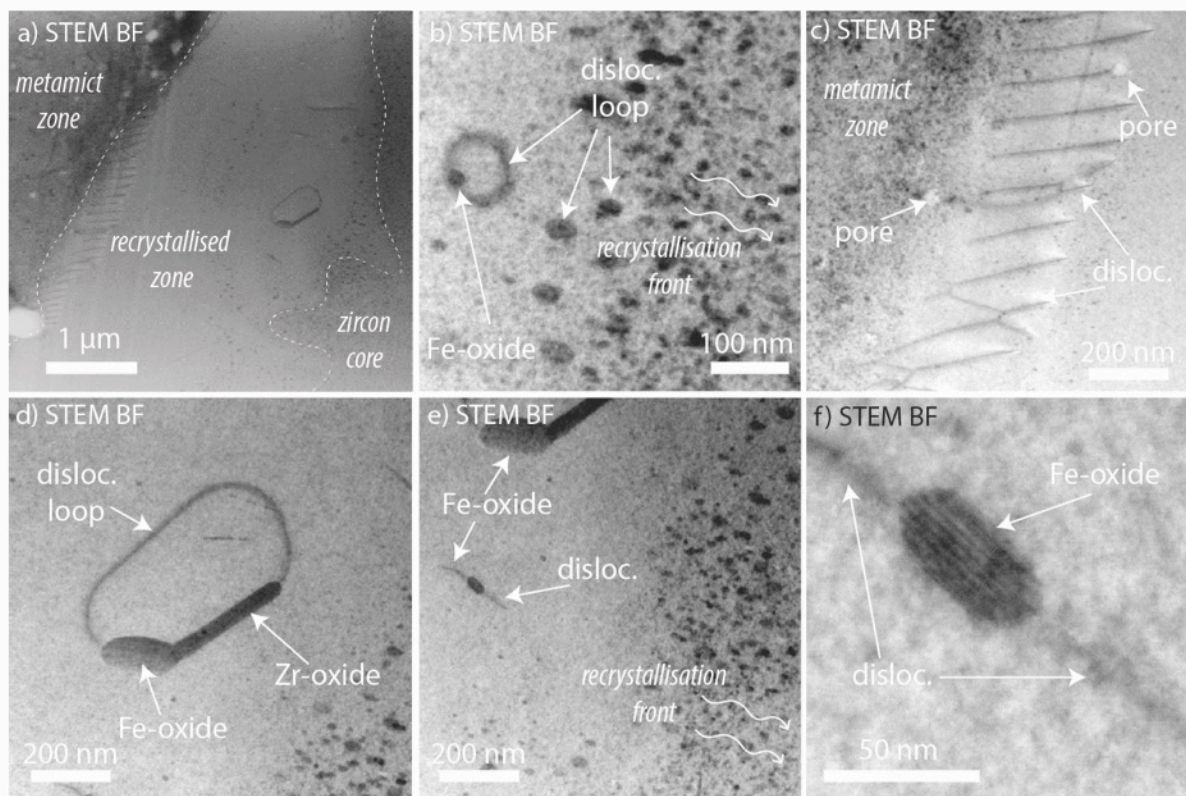
Oscillatory zoned core “recovery zone”



Supplementary Figure S4. STEM images of TEM foil extracted from Grain B core. Overview is from main text figure 1j and shows the majority of the sample, centre and RHS as oscillatory zoned with two crystal faces present. Each pair show a BF and HAADF image of a target area to highlight typical features and sizes. All inclusions are on secondary features but are clearly shown to be within primary oscillatory zoning. a-b) Images show the common “string of pearls” configuration seen in zones that have recovered from minor radiation damage (main text Figure 3). Pore spaces, accommodating the volume expansion, are joined by dislocation features. This setup provides a favorable scenario for pipe diffusion of Fe into sink regions (main text Figure 2f). c-d) Images

showing the partially filled pores with a variety of typical inclusion chemistries. Infilling of Fe and Ti is facilitated by dislocations acting as diffusion pathways into the oscillatory zoned interior of the grain. e-f) Examples of some of the largest magnetite grains associated with dislocations observed in this study. TEM tilt analysis gives maximum dimensions of 200×110 nm for the upper, octahedral grain (Fe_#21 in Supplementary Table 1; see Supplementary Information D for micromagnetic simulations of this particle).

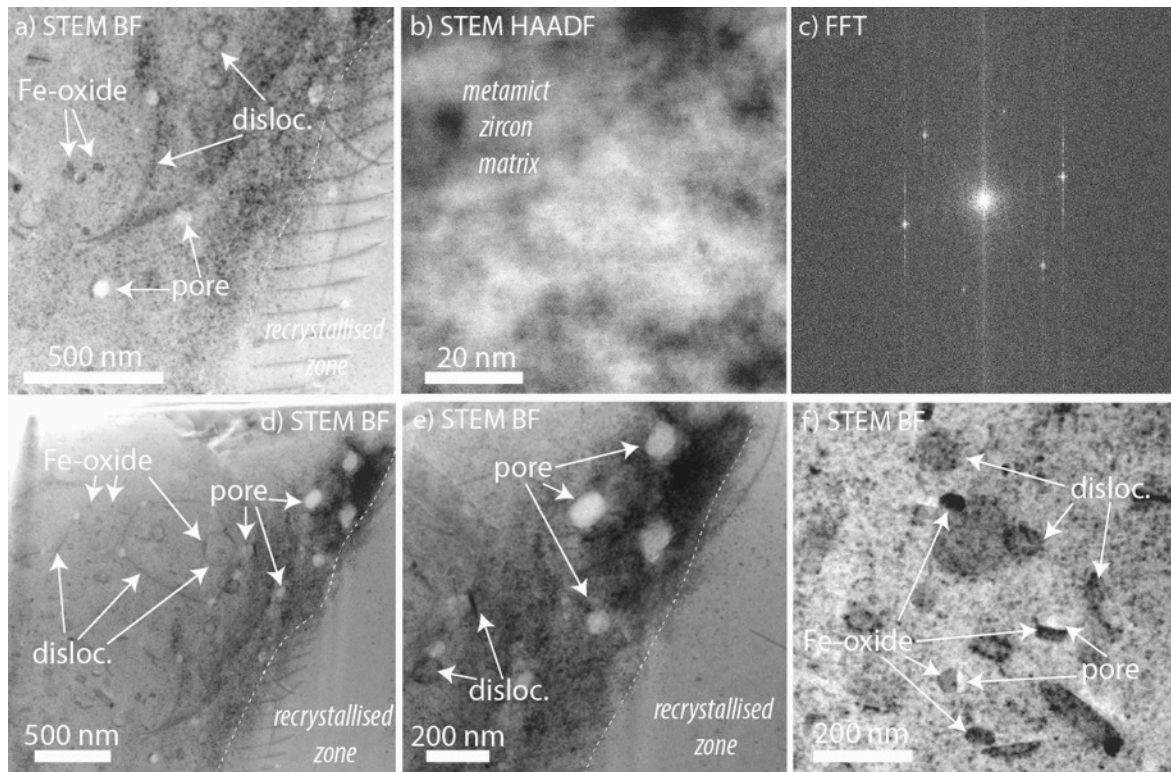
Fluid-assisted recrystallization zone



Supplementary Figure S5. STEM-BF images of TEM foil extracted from Grain B recrystallised zone. a) Overview of the recrystallised zone. Zircon matrix has undergone a fluid assisted diffusion-reaction process that has removed primary zoning but left behind a magnetite-bearing microstructure. Recrystallised zone is bounded to the right by the oscillatory zoned core, and to the left by the high U metamict zone, that may serve as a fluid ingress pathway. b) Boundary between the recrystallised zone and zircon core. This sinuous region is dominated by nanoscale dislocation loops resulting from the recrystallization process. Loops appear to increase in size away from the front and may be decorated with Fe-oxides in a “diamond ring” structure. c) Boundary between recrystallised zone and metamict area. This area displays stacked dislocation features and some associated porosity. d) The core of the recrystallised zone typically displays fewer, larger features than the boundaries. This large dislocation loop is the site of an Fe-oxide >150 nm in length and an elongate baddeleyite crystal (Fe_#32 in Supplementary Table 1; see Supplementary Information D for micromagnetic simulations

of this particle). e-f) Two magnifications of secondary Fe-oxide grains displaying the typical elongate nature, having grown with long axis parallel to associated dislocation features.

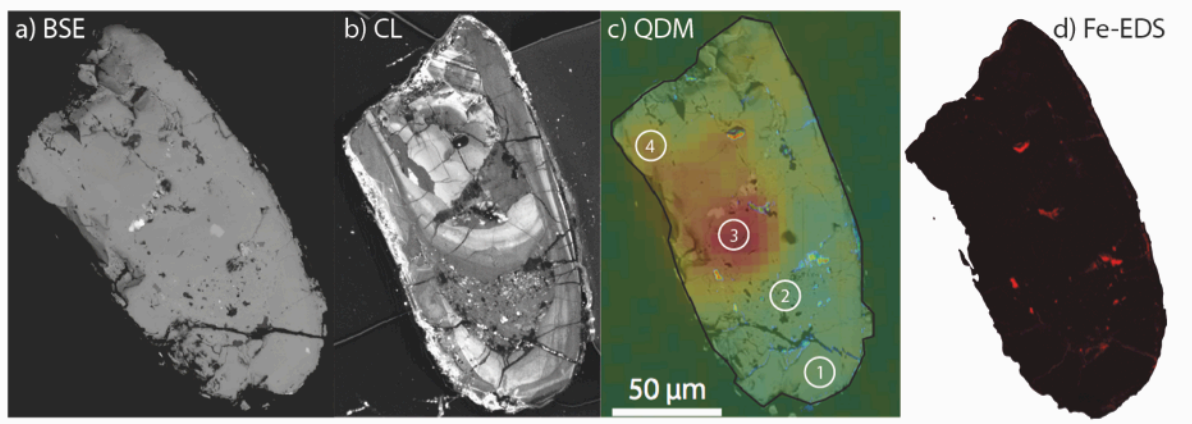
High U metamict zone



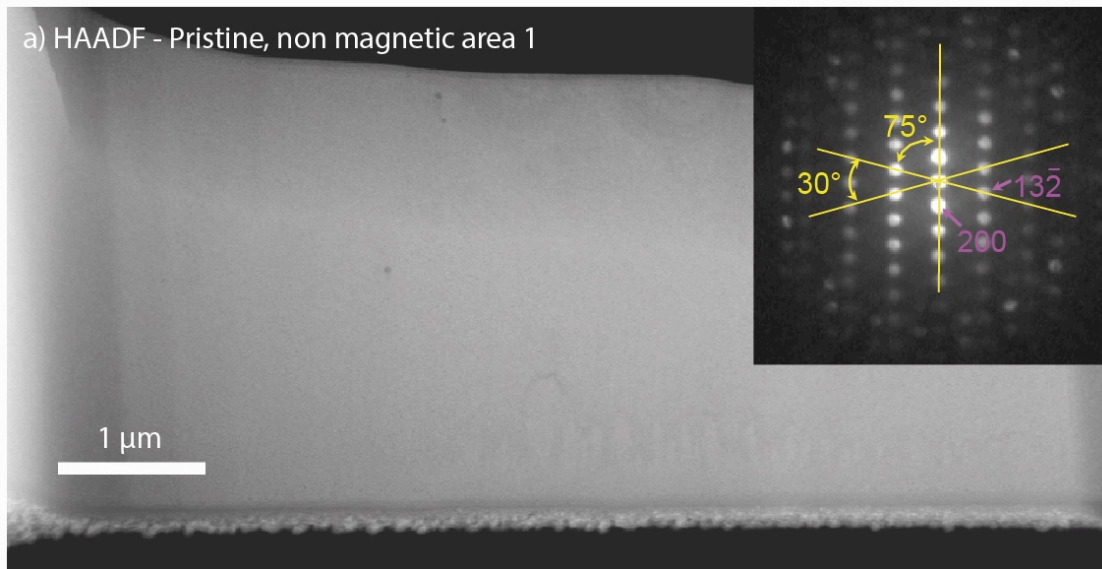
Supplementary Figure S6. STEM images of TEM foil extracted from Grain B metamict zone zone. a) Overview of the metamict zone. The zircon matrix in this area shows a more mottled appearance, indicative of higher degrees of radiation damage than has occurred in other parts of the grain, including loss of primary zoning. Whilst characterisation of this area was not a priority – due to highly damaged grains not being good paleomagnetic targets – the features present are still of general interest in relation to the recrystallization processes at work. Evidence of recovery of radiation damage is present in the form of pore space and dislocations, though of a higher density than seen in the grain core. Fe-oxide particles are associated with these features as seen in other areas. b) Close up image of the mottled texture of the zircon matrix. c) Fast fourier transform (FFT) of previous image demonstrates that the matrix is at least semi crystalline. This suggests that metamictisation has left islands of more pristine zircon, or that the matrix has recrystallised during fluid assisted processes. The latter is supported by the microstructures seen. d-f) Images at a variety of scales showing the density and relationship of microstructures and associated Fe-oxide particles. Additional work on grain C suggests metamict zone Fe-oxides may be dominated by hematite.

Grain C

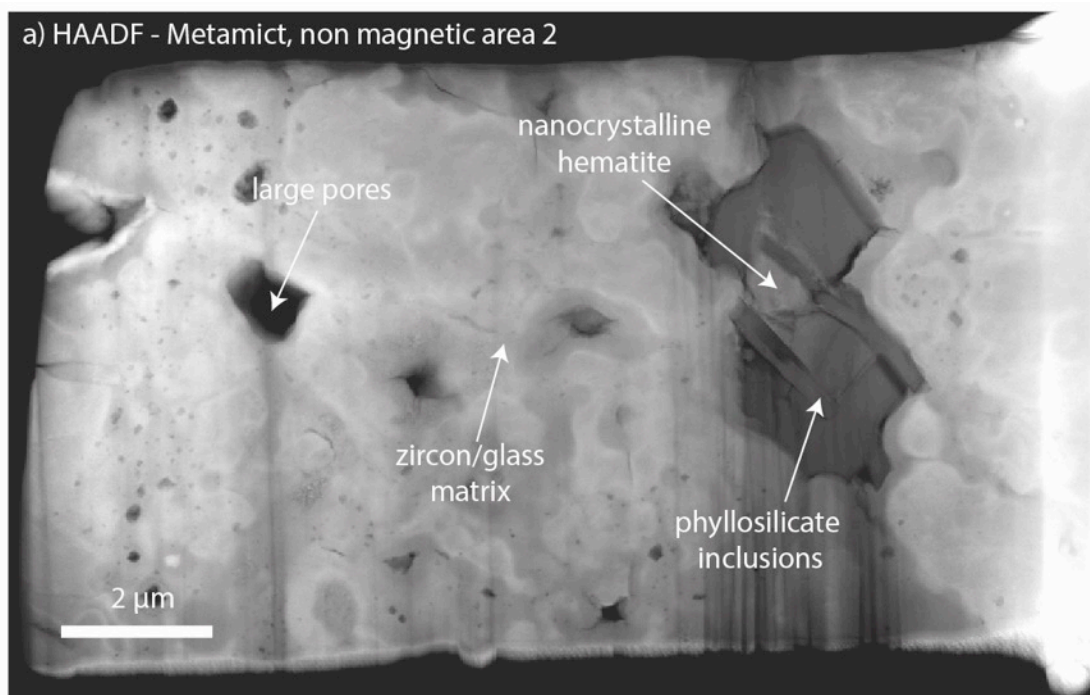
Grain C was the subject of an initial Jack Hills TEM study due to the presence of magnetic zones observed through QDM. This grain appears in the Weiss et al. (2018) study in Fig DR11D. Grain C contained a full range of internal zircon features, including the recovery and recrystallization zones from Grains A and B, but also pristine zircon with no magnetic signal, and fully metamict zones. This grain had not gone through the strict selection criteria for single crystal paleomagnetism, and was not dated. It was therefore used to characterise the full range of microstructural features typically present in Jack Hills zircons. And also provides evidence the microstructures are not the result of experimental heating during the paleomagnetic experiments undergone by Grains A and B.



Supplementary Figure S7. SEM and magnetic images of Grain C. Left to right: BSE, CL, QDM, Fe-EDS. QDM images show the locations of target areas of interest for preliminary TEM study. 1) Pristine BSE area with no magnetic signal 2) Metamict zone with high radiation damage and no magnetic signal. 3) Strongly magnetic region. 4) Weakly magnetic region. Apart from the metamict, zone all other regions show a lack of Fe hotspots in the EDS map.

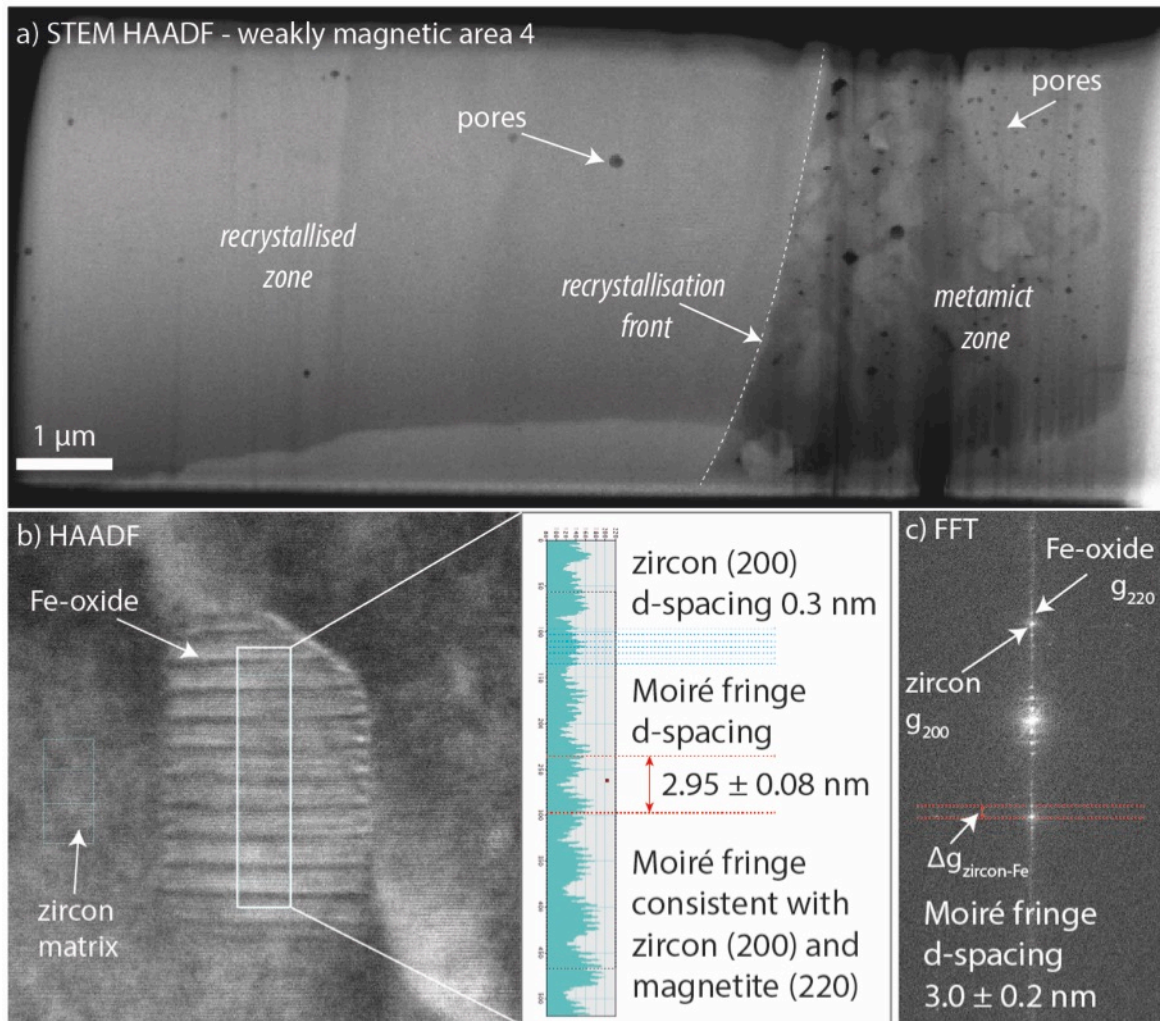


Supplementary Figure S8. HAADF image of TEM foil extracted from Grain C Area 1 – a pristine, non-magnetic area. Inset image shows a cropped TEM diffraction pattern of zircon $\langle 0-2-3 \rangle$ zone axis. This sample showed a small number of pores, just visible in the image above and a very low dislocation density. It is difficult to discern whether this sample represents truly pristine original zircon due to lack of zoning – which may be due to the $\langle 0-2-3 \rangle$ orientation – and instead may show a zone that has undergone recrystallization subsequent to a lesser degree of radiation damage than other areas. This sample nevertheless provided a critical test of the sensitivity of the QDM selection method: a lack of QDM signal correlates with an absence of Fe-oxide particles.



Supplementary Figure S9. HAADF image of TEM foil extracted from Grain C Area 2 – a metamict, non-magnetic area. Matrix comprises a highly heterogeneous mixture of variably radiation-damaged host zircon and secondary inclusions. This results in a complex looking image of variable brightness with a patchy nature, far beyond that seen in the main grains in this study (compared to the more metamict zones in Grain A). Pores appear dark in image and range from tens to hundreds of nm to microns in size. Pore spaces can accommodate a range of secondary inclusions, such as large biotite-chlorite grains that enclose nanocrystalline hematite, a likely source of Fe in the EDS images of metamict zones or micro/nanogranite inclusions. Nanocrystalline structure of hematite, identified through diffraction analysis of TEM sample, is diagnostic of secondary precipitation. No magnetic particles are detected by QDM in this sample or observed in the images.

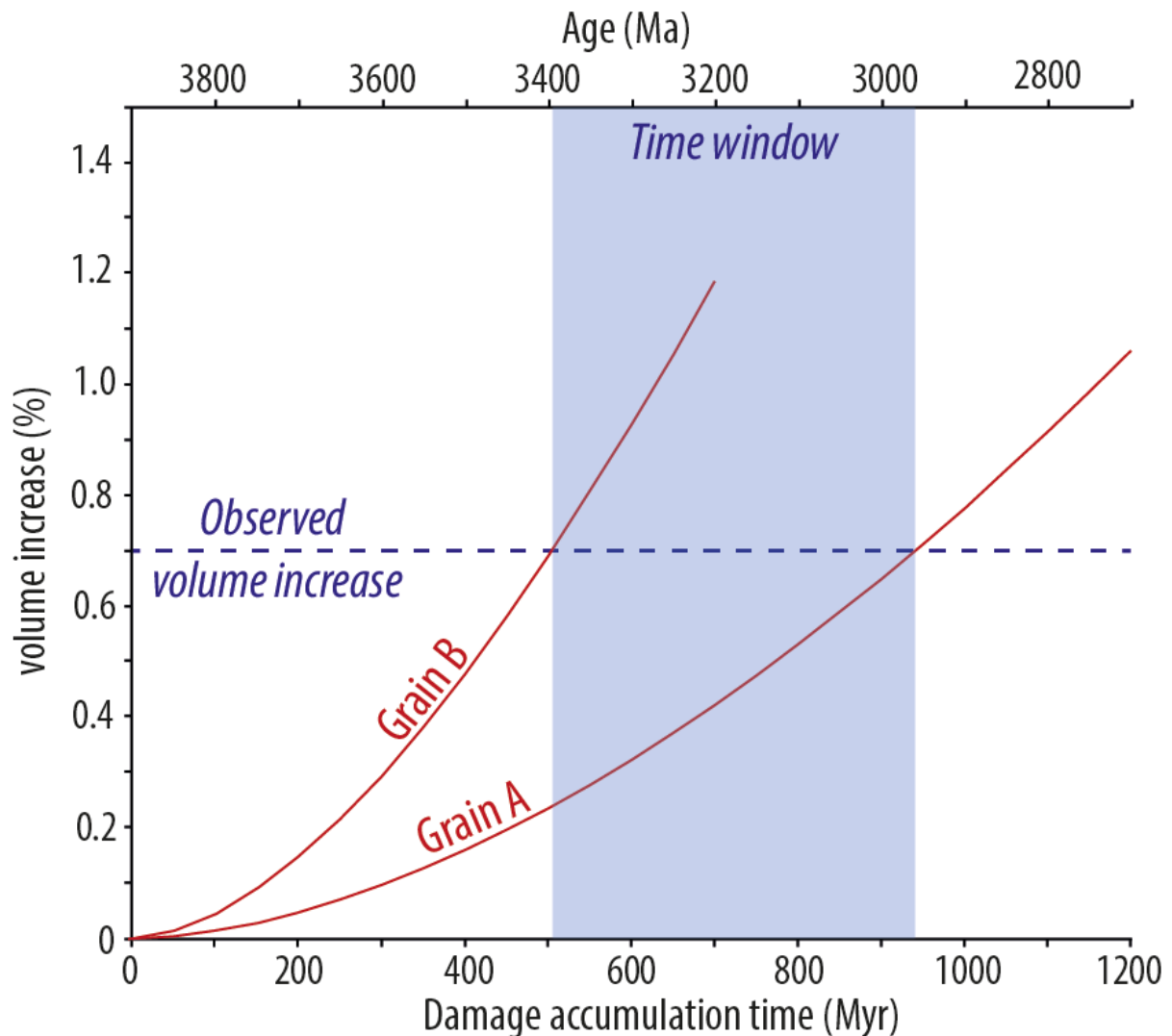
microstructures similar to Grain A. Oscillatory zoning is visible, along with pores, filled pores, and dislocations associated with radiation damage recovery. b) Larger scale view demonstrating partially filled pores containing Fe-oxides. c-d) HAADF images of same Fe-oxide particle at different tilt angles. Tilt analysis allows grain dimensions to be accurately calculated, and highlights inclusion position along dislocation feature. e) Example of STEM EDS output showing chemical analysis of inclusions. EDS spectra is mixed analysis of zircon host and Fe-oxide.



Supplementary Figure S11. STEM images of TEM foil extracted from Grain C Area 4 – a weakly magnetic area. a) HAADF image of whole TEM foil showing microstructures similar to Grain B. Left hand side is predominantly material showing no evidence of primary igneous zonation. Pore spaces are present, and the lack of zonation behind the curved front suggests fluid-assisted recrystallization. Right hand side is a metamict zone/layer with high porosity. Fluid recrystallization front may be advancing into the metamict zone b) Fe-oxide particle from main text Figure 2d. Figure shows calculation of Moiré fringe spacing at ~3 nm superimposed on the zircon (200) lattice plane. Moiré fringe spacing is indicative of magnetite or maghemite (220) lattice plane interference, and is not compatible with hematite. Magnetic data (Supplementary Information C) demonstrates that magnetite

is the Fe-oxide phase present and not maghemite. d) FFT of image data provides another mechanism for measuring Moiré fringe d -spacing and confirms zircon-magnetite relationship.

Supplementary information B – Radiation damage model

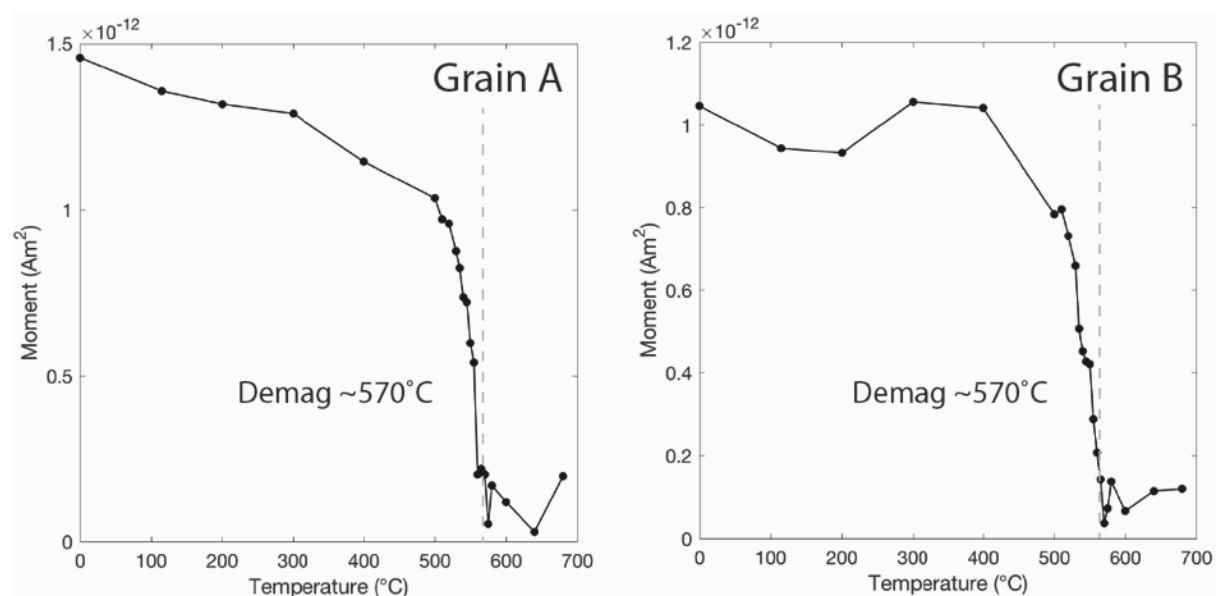


Supplementary Figure S12. Radiation damage model for zircon grains in this study. Image analysis of the porosity in the Jack Hills zircon grains shows approximately 0.7 % increase in the volume of the grain. This volume expansion, caused by the radiation damage associated with U and Th decay is time dependent, and can be converted into time taken to accumulate the damage (Murakami et al., 1991). Red lines show the gradual increase in volume through time for the specific U and Th contents of the two grains, and the time when they cross the observed 0.7 % volume increase. The region of the TEM image for grain A has had original actinide concentrations calculated as 224 ppm U and 171 ppm Th (Th/U = 0.76) and for grain B contained 434 ppm U and 282 ppm Th (Th/U = 0.65). These are typical Th/U ratios for igneous zircon in general (Kirkland et al, 2016). For these concentrations, the time taken to generate a 0.7% volume increase for grains A and B is *c.* 500 and *c.* 950 Myr

respectively, with both grains being *c.* 3900 Ma in age. This value corresponds to less than $\sim 10^{18}$ alpha decay events, meaning that the level of radiation damage being accommodated at this point is below even the first radiation damage percolation threshold. This timeframe is a lower estimate in the time taken to form the secondary magnetite crystals for several reasons. i) The image analysis did not account for small voids (<10 nm) that are numerous and just visible in the TEM images. ii) We cannot account for pore volumes that have already been accommodated by some level of structural recovery by the formation of dislocations. iii) This only accounts for the formation of space to accommodate the Fe influx, and so magnetite formation can only be determined to be later than the pore formation. Fe-influx and magnetite formation may be due to specific geological events, or a continuous process of influx throughout geological time.

Supplementary information C – Paleomagnetic (demag) data

Measurements of the paleomagnetic data were conducted at the MIT Paleomagnetic Laboratory using the Superconducting Quantum Interference Device (SQUID) microscope (Weiss et al, 2007). Measurements of the magnetic moments of grains A and B followed the protocols from Fu et al, (2017). These data sets are available upon request, and are part of a bigger dataset of paleomagnetic data of the Jack Hills detrital zircon grains to be published in the future.



Supplementary Figure S13. Thermal demagnetisation of natural remanent magnetisation of grains A and B, obtained using the scanning SQUID microscopy method of Fu et al. (2017) and Weiss et al. (2018). Rapid demagnetisation occurring in the temperature range 500-570 °C is consistent with the presence of abundant single-domain to vortex-state particles of magnetite observed here with TEM, and with the distribution of blocking temperatures derived from the size and shape of the observed particles using micromagnetic simulations (see Supplementary Information D).

Supplementary Information D – Micromagnetic Modelling

Indicative thermal blocking temperatures (T_B) were calculated using the following assumptions and approximations. Each particle was assumed to be in the single-domain state with uniaxial shape anisotropy. The three-dimensional shape of each particle was approximated as either an ellipsoid of revolution or a square-based prism, as indicated by the labels ‘ellipse’ and ‘rectangular’, respectively, in Supplementary Table 1. The aspect ratio of each particle was taken to be L/W . The relationship between T_B and t_{obs} was calculated using the method of Pullaiah et al. (1975):

$$\frac{T_B \ln\left(\frac{t_{\text{obs}}}{\tau_0}\right)}{\beta^2(T_B)} = \frac{VM_s(298)H_K(298)}{2k_B} \quad (\text{Eqn. 1})$$

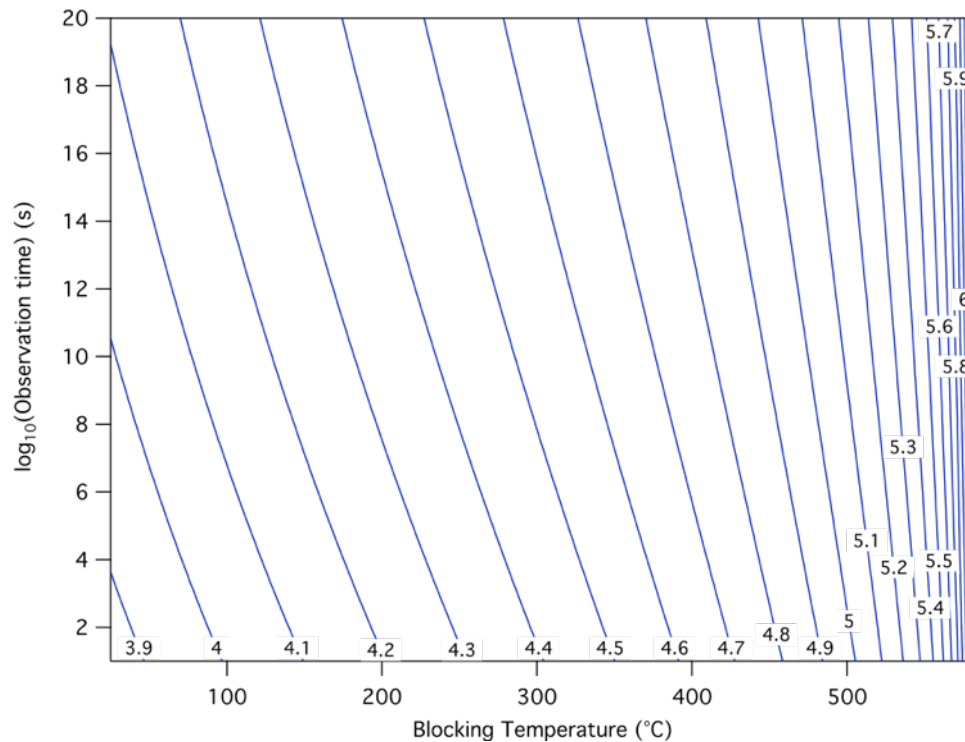
where t_{obs} is the observation time, τ_0 is the attempt time, V is particle volume, $M_s(298)$ is the room-temperature saturation magnetisation, $H_K(298)$ is the room-temperature microcoercivity, and k_B is the Boltzmann constant. The β factor defines the temperature dependence of saturation magnetisation:

$$\beta(T) = \frac{M_s(T)}{M_s(298)} = \left(\frac{T_c - T}{T_c - 298}\right)^{0.43} \quad (\text{Eqn. 2})$$

where T_c is the Curie temperature. Microcoercivity was calculated assuming shape anisotropy is dominant:

$$H_K(298) = M_s(298)\Delta N \quad (\text{Eqn. 3})$$

where ΔN is the difference in demagnetising factor between the short and long axes of the particle. Demagnetising factors were calculated according to Stoner (1945) and Aharoni (1998) for ellipsoids and square-based prisms, respectively. Values of $\tau_0 = 1 \times 10^{-10}$ sec, $M_s(298) = 480$ kA/m, and $T_c = 858$ K were used.



Supplementary Figure S14. Variation of blocking temperature as a function of the observation time for magnetite particles with a given combination of volume and microcoercivity. Contour labels correspond \log_{10} of the right-hand side of Eqn. 1 (referred to as ‘stability contour’ in Supplementary Table 1). Stability contour values > 5 are required for the preservation of Hadean remanence in the Jack Hills, corresponding to particles that have the potential to retain a primary remanence despite greenschist facies metamorphism of the host rocks to 346-487 °C for ~1-10 Myr (Rasmussen et al., 2010).

Blocking temperatures for the two particles plotting above the single domain to vortex threshold (Fe_#21 and Fe_#32 in Supplementary Table 1; Supplementary Figure 4e and Supplementary Figure 5d) were calculated using micromagnetic simulations according to the method of Nagy et al. (2017). Calculations were performed using the MERRILL finite-element code (Conbhuí et al.). The grain geometries were defined using linear tetrahedral elements with an average edge length of 8nm (c.f. the exchange length for magnetite of 9nm). Energy barriers were calculated using the nudged elastic band (NEB)/ minimum action method of Fabian and Shcherbakov (2017). Particle Fe_#21 was approximated as an elongated octahedron with minor truncations to create small {001} type faces at the apices of the octahedron (Supplementary Movie S15). Particle Fe_#32 was modelled as an ellipsoid of revolution (Supplementary Movie S16). Particle Fe_#21 adopts a uniformly magnetised remanence state, with easy axis aligned with elongation direction of the octahedron. Particle Fe_#32 is a single-vortex state at remanence, with vortex core aligned with the elongation direction of the

ellipsoid. In both cases, the magnetisation reversal mechanism involves the formation and rotation of a single-vortex state, with the vortex core being forced to rotate across the short-axis of the particle. This traverse of the short axis by the vortex core results in a large energy barrier for magnetisation reversal, and a correspondingly high blocking temperature ($T_B = 570$ °C for Fe_#21 and $T_B = 575$ °C for Fe_#32, assuming 100 sec laboratory observation times). These values are close to those obtained using the single-domain approximation ($T_B = T_c = 585$ °C for Fe_#21 and $T_B = 582$ °C for Fe_#32; Supplementary Table 1), although single-domain theory clearly misrepresents the reversal mechanism and exact nature of the domain states. In order to isolate putative primary Hadean paleomagnetism, thermal demagnetisation to a temperature of 565 °C is used (Tarduno et al., 2015). These simulations demonstrate, however, that such a procedure is not capable of removing the younger secondary component of CRM carried by magnetite particles formed during recrystallisation and recovery.

Movie Legends

Movie S15. Micromagnetic simulation of magnetic reversal in particle #21 (elongated tetrahedron) showing formation and rotation of single domain vortex state. Modelling determines a large energy barrier for magnetic reversal as the vortex core is forced to rotate across the short axis of the particle. Upper panel) Three grain orientations showing orientation of vortex core only. Lower panel) Three grain orientations showing full micromagnetic simulation.

Movie S16. Micromagnetic simulation of magnetic reversal in particle #32 (ellipsoid of revolution) showing formation and rotation of single domain vortex state. As with the previous example, modelling determines a large energy barrier for magnetic reversal as the vortex core is forced to rotate across the short axis of the particle. Upper panel) Three grain orientations showing orientation of vortex core only. Lower panel) Three grain orientations showing full micromagnetic simulation.

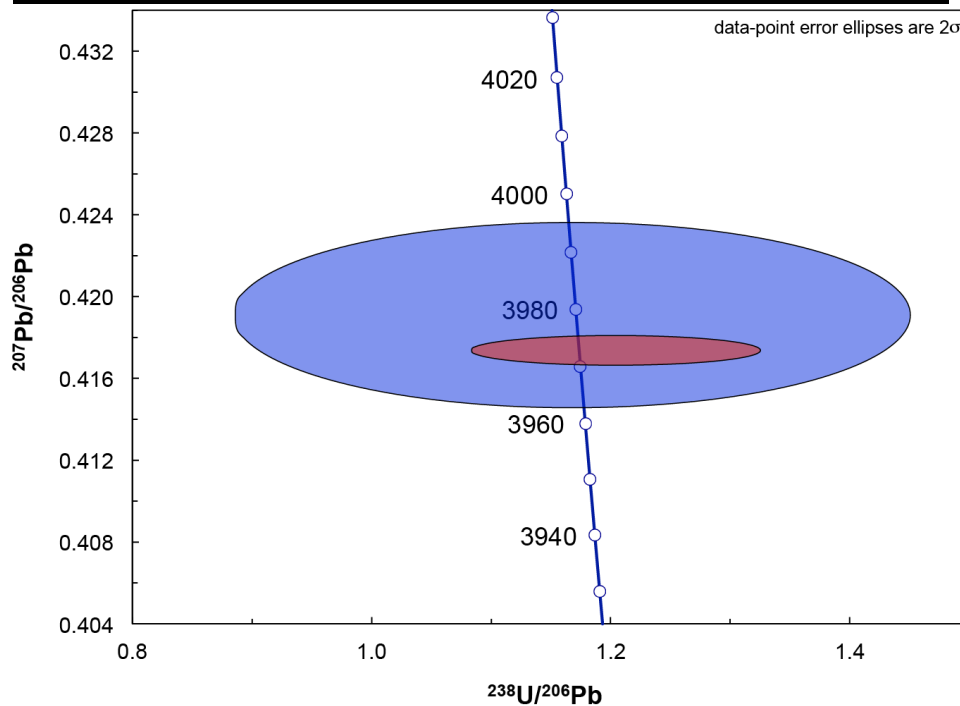
Supplementary Information E – Uranium-Lead dating

Zircon grains were analysed during U-Pb sessions on the Cameca IMS 1270 Ion Microprobe at UCLA during sessions on 9/5/2017 (Grain A) and 7/7/2016 (Grain B). The instrument was operated under standard procedures for the collection of U and Pb isotopes. U-Pb isotopic measurements were calibrated against multiple analyses of standard reference material AS3 (Paces and Miller, 1993) throughout the analytical sessions.

Isotopic data for the 2 grains in this study are in the table below. This includes ages and isotopic ratios for $^{206}\text{Pb}/^{238}\text{U}$, $^{207}\text{Pb}/^{235}\text{U}$ and $^{207}\text{Pb}/^{206}\text{Pb}$ along with calculated 1 s.e. uncertainties. Values of concordance have also been calculated in terms of deviation of the datapoint centroid from the concordia curve for Pb-Pb (defined as % difference of $^{206}\text{Pb}/^{238}\text{U}$ and $^{207}\text{Pb}/^{206}\text{Pb}$ ages) and U-Pb

(defined as % difference of $^{206}\text{Pb}/^{238}\text{U}$ and $^{207}\text{Pb}/^{206}\text{Pb}$ ages) with a maximum value of 4%. Both analyses fit a true definition of concordance in that the 2 sigma error ellipse overlaps the concordia curve (Spencer et al, 2016). Common Pb corrections (based on measured ^{204}Pb) are minor with a calculated radiogenic Pb component of ~99.9% in both grains. Data table and Tera-Wasserburg concordia plot are shown below. Grain A in Blue, Grain B in Red.

Name	Cambridge	<i>manuscript</i>		Grain A	Grain B
Name	MIT	<i>paleomag</i>		080211_h30	071320_h02
Name	UCLA	<i>UPb</i>		UCLA 8_2_11.ais	UCLA 7_13_20.ais
Age (Ma)	206Pb/	238U		3990	3899
error (Ma)	206Pb/	238U	1 s.e.	297	121
Age (Ma)	207Pb/	235U		3983	3948
error (Ma)	207Pb/	235U	1 s.e.	100	41
Age (Ma)	207Pb/	206Pb		3979	3973
error (Ma)	207Pb/	206Pb	1 s.e.	7	1
Concordance	Pb-Pb		%	0	2
	U-Pb		%	0	1
Ratio	207Pb*/	235U		49.52	47.80
error	207Pb*/	235U	1 s.e.	4.96	1.98
Ratio	206Pb*/	238U		0.86	0.83
error	206Pb*/	238U	1 s.e.	0.09	0.03
Correlation of concordia ellipses				1.00	1.00
Ratio	238U/	206Pb*		1.17	1.20
error	238U/	206Pb*	1 s.e.	0.12	0.01
Ratio	207Pb*/	206Pb*		0.42	0.42
error	207Pb*/	206Pb*	1 s.e.	0.002	0.0003
Common	206Pb/	204Pb		18.86	18.86
Common	207Pb/	204Pb		15.62	15.62
Common	208Pb/	204Pb		38.34	38.34
Pb corr.				(204Pb)	(204Pb)
% Radiogenic	206Pb			99.89	99.95



Supplementary References

- Aharoni, A., 1998. Demagnetizing factors for rectangular ferromagnetic prisms. *Journal of applied physics*, 83(6): 3432-3434.
- Conbhuí, P.Ó. et al., MERRILL: Micromagnetic Earth Related Robust Interpreted Language Laboratory. *Geochemistry, Geophysics, Geosystems*.
- Fabian, K., Shcherbakov, V.P., 2017. Energy barriers in three-dimensional micromagnetic models and the physics of thermo-viscous magnetization in multidomain particles. arXiv preprint arXiv:1702.00070.
- Fu, R.R. et al., 2017. Evaluating the paleomagnetic potential of single zircon crystals using the Bishop Tuff. *Earth and Planetary Science Letters*, 458: 1-13.
- Kirkland, C.L., et al., 2015. Zircon Th/U ratios in magmatic environs. *Lithos*, 212, pp.397-414.
- Murakami, T., Chakoumakos, B.C., Ewing, R.C., Lumpkin, G.R., Weber, W.J., 1991. Alpha-decay event damage in zircon. *American Mineralogist*; (United States), 76.
- Muxworthy, A.R., Williams, W., 2008. Critical superparamagnetic/single-domain grain sizes in interacting magnetite particles: implications for magnetosome crystals. *Journal of the Royal Society Interface: rsif*. 2008.0462.
- Nagy, L. et al., 2017. Stability of equidimensional pseudo–single-domain magnetite over billion-year timescales. *Proceedings of the National Academy of Sciences*, 114(39): 10356-10360.
- Paces, J.B. and Miller Jr, J.D., 1993. Precise U-Pb ages of Duluth complex and related mafic intrusions, northeastern Minnesota: Geochronological insights to physical, petrogenetic, paleomagnetic, and tectonomagmatic processes associated with the 1.1 Ga midcontinent rift system. *Journal of Geophysical Research: Solid Earth*, 98(B8), pp.13997-14013.
- Pullaiah, G., Irving, E., Buchan, K., Dunlop, D., 1975. Magnetization changes caused by burial and uplift. *Earth and Planetary Science Letters*, 28(2): 133-143.
- Rasmussen, B., Fletcher, I.R., Muhling, J.R., Wilde, S.A., 2010. In situ U-Th-Pb geochronology of monazite and xenotime from the Jack Hills belt: Implications for the age of deposition and metamorphism of Hadean zircons. *Precambrian Research*, 180(1-2): 26-46.
- Spencer, C.J., Kirkland, C.L. and Taylor, R.J., 2016. Strategies towards statistically robust interpretations of in situ U–Pb zircon geochronology. *Geoscience Frontiers*, 7(4), pp.581-589.
- Stoner, E.C., 1945. XCVII. The demagnetizing factors for ellipsoids. *The London, Edinburgh, and Dublin philosophical magazine and journal of science*, 36(263): 803-821.
- Tarduno, J.A., Cottrell, R.D., Davis, W.J., Nimmo, F., Bono, R.K., 2015. A Hadean to Paleoproterozoic geodynamo recorded by single zircon crystals. *Science*, 349(6247): 521-524.
- Weiss, B.P. et al., 2018. Secondary magnetic inclusions in detrital zircons from the Jack Hills, Western Australia, and implications for the origin of the geodynamo. *Geology*.

Supplementary Table 1

Grain A	Ref.	L (nm)	Error	W (nm)	Error	Ratio (L/W)	Error	Approx. Shape	Location	Stability Contour	TB°C [100 sec]
Box 1	Fe_#1	122	3	21	2	5.8	0.6	Rectangular		5.34	549
	Fe_#2	43	3	20	2	2.2	0.3	Rectangular	Pore	4.60	384
	Fe_#3	63	4	45	3	1.4	0.1	Rectangular	Dislocation	5.15	528
	Fe_#4	39	3	12	3	3.3	0.9	Rectangular		4.25	221
	Fe_#5	59	4	33	4	1.8	0.2	Rectangular	Pore	5.07	515
	Fe_#6	46	3	17	3	2.7	0.5	Rectangular	Dislocation	4.57	375
Box 2	Fe_#7	81	4	36	3	2.3	0.2	Rectangular	Pore	5.40	554
	Fe_#8	38	3	12	3	3.2	0.8	Rectangular		4.23	212
	Fe_#9	37	3	9	2	4.1	1.0	Rectangular	Dislocation	4.03	104
	Fe_#10	33	4	15	3	2.2	0.5	Rectangular		4.24	216
	Fe_#11	30	3	11	2	2.7	0.6	Rectangular	Dislocation	4.01	95
	Fe_#12	42	4	40	3	1.1	0.1	Rectangular	Pore	4.06	117
	Fe_#13	31	4	17	3	1.8	0.4	Rectangular		4.23	207
	Fe_#14	59	3	21	2	2.8	0.3	Rectangular	Dislocation	4.88	475
	Fe_#15	52	4	37	3	1.4	0.2	Rectangular	Pore	4.90	481
Box 3	Fe_#16	68	3	9	2	7.6	1.7	Rectangular	Pore	4.37	283
	Fe_#17	55	5	47	5	1.2	0.2	Ellipse	Pore and dislocation	4.61	389
	Fe_#18	45	3	44	3	1.0	0.1	Ellipse		3.63	SP
	Fe_#19	50	2	8	2	6.3	1.6	Rectangular	Dislocation	4.12	150
	Fe_#20	56	2	12	2	4.7	0.8	Rectangular		4.48	334
Grain B	Ref.	L (nm)	Error	W (nm)	Error	L/W	Error	Approx. Shape	Location	Stability Contour	TB°C [100 sec]
Recovery zone	Fe_#21	200	4	118	3	1.69	0.05	Ellipse	Pore	6.46	585
	Fe_#22	130	4	110	3	1.18	0.05	Ellipse	Pore and dislocation	5.75	572
	Fe_#23	70	3	46	3	1.52	0.12	Ellipse		5.10	520
	Fe_#24	68	3	47	3	1.45	0.11	Ellipse	Dislocation	5.06	513
	Fe_#25	35	3	30	3	1.17	0.15	Ellipse		4.02	98
	Fe_#26	50	4	40	3	1.25	0.14	Ellipse		4.58	377
	Fe_#27	65	4	57	4	1.14	0.11	Ellipse	Pore	4.78	447
	Fe_#28	70	4	50	3	1.40	0.12	Rectangle	Pore	5.29	544
	Fe_#29	53	3	29	3	1.83	0.22	Rectangle	Pore	4.92	485
	Fe_#30	80	3	51	3	1.57	0.11	Ellipse	Pore	5.28	543
Recrystallized zone	Fe_#31	26	3	18	3	1.44	0.29	Ellipse		3.80	SP
	Fe_#32	184	7	87	5	2.11	0.15	Ellipse	Dislocation	6.29	582
	Fe_#33	13	3	9	2	1.44	0.46	Ellipse	Inclusion in ZrO2	2.90	SP
	Fe_#34	54	3	25	3	2.16	0.29	Rectangle	Dislocation	4.89	477
	Fe_#35	24	3	22	2	1.09	0.17	Ellipse	Dislocation	3.34	SP
Metamic zone	Fe_#36	28	3	25	3	1.12	0.18	Ellipse	Pore	3.63	SP
	Fe_#37	48	3	30	3	1.60	0.19	Ellipse	Pore	4.61	389
	Fe_#38	40	3	35	3	1.14	0.13	Ellipse	Dislocation	4.15	167
	Fe_#39	44	3	27	3	1.63	0.21	Ellipse	Pore	4.50	342
	Fe_#40	45	3	31	3	1.45	0.17	Ellipse	Pore	4.52	351
Grain C Lamella 1	Ref.	L (nm)	Error	W (nm)	Error	L/W	Error	Approx. Shape	Location	Stability Contour	TB°C [100 sec]
Recrystallized zone	Fe_#41	20	2	14	2	1.43	0.25	Rectangular	Dislocation	3.66	SP
	Fe_#42	32	2	20	2	1.60	0.19	Rectangular	Dislocation	4.29	239
	Fe_#43	21	2	16	2	1.31	0.21	Rectangular		3.69	SP
	Fe_#44	29	2	13	2	2.23	0.38	Rectangular	Dislocation	4.07	124
Grain C Lamella 2	Ref.	L (nm)	Error	W (nm)	Error	L/W	Error	Approx. Shape	Location	Stability Contour	TB°C [100 sec]
Recrystallized zone	Fe_#145	32	2	20	2	1.60	0.19	Rectangular	Pore	4.29	239
	Fe_#46	25	2	22	2	1.14	0.14	Ellipse	Pore	3.52	SP
	Fe_#47	50	2	17	2	2.94	0.37	Rectangular	Dislocation	4.64	399
	Fe_#48	25	2	12	2	2.08	0.39	Ellipse	Pore	3.70	SP
	Fe_#49	26	2	12	2	2.17	0.40	Rectangular	Dislocation	3.94	57
	Fe_#50	35	2	9	2	3.89	0.89	Rectangular	Dislocation	4.00	86
	Fe_#51	22	2	21	2	1.05	0.14	Ellipse	Pore	3.00	SP
	Fe_#52	26	2	23	2	1.13	0.13	Ellipse	Pore	3.56	SP
	Fe_#53	46	2	20	2	2.30	0.25	Rectangular	Pore	4.66	406
	Fe_#54	22	2	15	2	1.47	0.24	Rectangular	Dislocation	3.79	SP
	Fe_#55	30	2	22	2	1.36	0.15	Rectangular	Pore and dislocation	4.18	180
Grain C Lamella 3	Ref.	L (nm)	Error	W (nm)	Error	L/W	Error	Approx. Shape	Location	Stability Contour	TB°C [100 sec]
Recrystallized zone	Fe_#56	63	2	27	2	2.33	0.188	Rectangular		5.06	513

Dr. R.J.M. Taylor
Dept. of Earth Sciences
University of Cambridge
Downing Street
Cambridge, CB2 3EQ
England

e-mail: rjt79@cam.ac.uk
tel: +44 (0) 1223 333433

31 October 2018

Dear Editor,

We would like to submit the revised article “Secondary magnetite in ancient zircon precludes analysis of a Hadean geodynamo”, by F. Tang *et al.*, for consideration by PNAS.

We thank the two reviewers for their constructive and knowledgeable comments, resulting in a number of improvements to the text. We believe this work makes a considerable addition to the field and the fact that both reviewers agreed with the central tenet of the manuscript, that the magnetisation is secondary, is a very positive result.

The main criticism from both reviewers has been remedied. A data table and concordia diagram has been included for the two grains. The two grains in question are in fact greater than the 90% concordance figure that was used for the project as a whole. Additional text has also been added into the methods section to describe the data collection.

We have carefully assessed all the additional comments made by the reviewers. We have outlined our thorough responses to each query in the text below. Original reviewer comments are in italics, and our response below.

Reviewer 1

There is a glaring problem with this manuscript as submitted- there are no U/Pb data presented! This is a bizarre omission, given that the claim is made (Line 79) that the grains are >90% concordant. This must be an oversight? If the data exist, why not cite at least Concordia intercept ages- this is relevant to any comparison with the zircons analyzed by Tarduno et al. Obviously the data must be presented.

We agree with both reviewers that this data is a useful and necessary addition. It was not originally included simply because the main focus of the manuscript was on the TEM results rather than the geochronology. However, we are very happy to include this data here, and a full isotopic data table from the UCLA SIMS sessions, including

concordia figure for the analyses on grains A and B has now been added to the supplementary information document as Supplementary Information E.

Lines 48-49. "... predate inner core solidification..." The timing of inner core solidification is not well-constrained, as suggested in later sentences. Any assertions about this are very model-dependent.

The reviewer is correct. The text has been amended to make it clear this is an assertion based on the majority of estimates from models. now reads "According to many core formation models..."

Line 118. "... zircon acquired..." Zircon per se doesn't acquire remanance- poor wording.

This text has been changed to make it clear it is the inclusions within zircon that acquire the TRM, not the zircon itself.

Line 163-167. "Evaluation of the TEM images..." Firstly, it is unclear what kind of evaluation leads to the conclusion of 0.7% expansion- is this simply the void space now observed?

The text has been amended here to make it clear this is an estimate based on the image analysis of pore volume within the TEM sample. This is a lower estimate of porosity as further explained in Supplementary Information B.

More importantly, why does the resulting inferred alpha dose suggest that the Fe source was JH sediment? This goes back to the question of what the U/Pb ages are ...

This is a good point. The radiation damage time to produce the observed porosity makes the accommodation space for the magnetite. In grain B the 500 Myr time frame means the original magmatic rocks may be the Fe source, however the 950 Myr timeframe for Grain A is post depositional age, and therefore allows for the source to be the sedimentary rock now hosting the zircon. This section has been expanded to clarify this distinction and range of possibilities. In either case, the age of the magnetite is significantly later than the crystallisation age of the zircon.

All in all I recommend publication with minor revision but certainly including addition of the U/Pb ion probe data.

Reviewer 2

With regard to the occurrence of magnetite it needs to be clearly stated whether the samples for TEM study were extracted from the grains before or after the grains were subjected to thermal demagnetization at over 500oC.

For grains A and B the images are taken after the heating experiments. Although there were strict criteria to ensure that no alteration was observed. This is confirmed by the analysis of Grain C (Supplemental Materials) which was not used for the paleomag intensity study, and had therefore not undergone any heating experiments, and showed

the same observable microstructures and secondary inclusions. This distinction has been added to the text prior to the description of microstructures.

Fig.2 shows selected structures and magnetite inclusions from grains A and B.

With regard to the TEM image of grain A on Fig1 are the white spot inclusions seen concentrated in the dark zones magnetite? How does this image (Fig.1i) relate to images in Supplementary Figure S2? where the secondary structures in grain A are much more comprehensively shown. Similarly regarding grain B. supplementary Figure S4,S5 and S6 provides a series of images on the secondary structures and inclusions, including their locations, whereas this information is not present on the TEM image in Fig.1. in the actual paper. Some images are shown on the composite Figure 2 but it would seem in the best interests of the paper to include images showing relevant secondary features such as shown in supplementary Figure 2 and supplementary Figures S4, S5 and S6 as separate figures for grains

In response to the first reviewer's comments, the manuscript has been lengthened, and therefore we are unfortunately unable to accommodate additional figures. Our figure layout in Fig. 2 and the Supplementary Figures was deliberate. Figure 2 is intended to show an example of each of the secondary microstructures and features, and, as such, includes images from Grain A and B, and also Grain C, which is supplemental only. This enables a quick compilation (for the reader) of all the different evidence that demonstrates a secondary magnetite origin in one place. The supplemental figures then go through each grain by textural setting and show multiple examples for the reader to assess each grain in more detail. We believe (from prior to original submission) that to transfer individual grain detail into the manuscript would result in lots of repetition of image types and lose the clarity of seeing each structure. We have edited the caption and text to make it clear which grain each of the images originates from.

With regard to the large white spots the reviewer has mentioned, these are low density areas (large pore spaces) associated with the more radiation damaged zones. As stated in the relevant Supplementary Information these more metamict zones are not associated with any observed magnetite, which are limited to the more crystalline regions of the grains.

Figure 3 . This figure shows the proposed development steps in the formation of secondary structures in Grain B. The evidence for the progressive development stages illustrated on the figure need to be discussed in the paper and supported by reference to relevant structures such as shown on Supplementary Figures 4,5 and 6. or Fig 3 should be dropped.

We have made a significant addition to the "Grain B" section to describe the progression of events depicted in figure 3, and link them to the additional images found in the Supplementary Information.

Further comments

It is not clear to the reviewer that the FeO phase described is magnetite? This is an important question when considering the origin of the secondary Fe. Magnetite is not found in low-temperature weathering products but the magnetic mineral maghemite is. Could the FeO phase in the Jack hills structures be maghemite? Further discussion of the evidence indicating that the FeO phase is magnetite is needed.

The combined evidence for magnetite is defined in the supplementary material. Additional text has been added to the main manuscript to clarify these observations. The TEM Moire fringe data is closest to the zircon-magnetite interference pattern, although we cannot definitively rule out maghemite using diffraction data alone, given the similarity in d-spacings between magnetite and maghemite. However, the paleomagnetic observation that the NRM demagnetization is complete by 580°C is only compatible with magnetite, as maghemite would persist to higher temperature, and show additional thermal alteration effects. The combination of diffraction and magnetic evidence supports the identification of magnetite.

Line 32 Is there a date for the remnant magnetism? If so this should be mentioned somewhere as it bears on models for the origin of the Fe.

There is no firm date for the magnetisation. Indeed, this is one of the key conclusions of the study. The magnetite particles identified are ideal magnetic recorders, but are not related to the zircon's crystallisation age. There is currently no way to obtain a meaningful age for the magnetisation. The radiation damage constraints are able to place an upper age limit, as the Fe must post-date the space accommodation, but no definitive age can be placed on magnetisation.

Where is the U-Pb isotopic data?

A table of U-Pb data is needed and the location of SIMs spots shown on grain images. It is not unknown that some parts of grains can be concordant whereas other parts are discordant. These data would also include U and Th concentrations and the common Pb content.

See earlier comment to reviewer 1. This data is now present in the supplementary information and referred to in the text.

It is noted that the grains are about 25µm in length. In the reviewer's experience these are very small. Jack Hills grains range up to and over 300µm in length. At 25 µm a Cameca U-Pb analysis would cover almost half the grain. Were these the only grains that fitted the criteria? A discussion on why these grains, which appear on the small side (and rather atypical in the case of grain B) , were chosen for this study would be helpful.

This statement is incorrect. The reviewer has mistaken the 25µm scale bar for the figure as representing the size of the whole grain. The grains themselves are 100's µm in length as suggested and are typical of the size of zircon grains in general.

Lines 81-83

"Three broadly defined textures were seen in the SEM images (i) primary oscillatory zoning (ii) recrystallized zones with bright CL (iii) strongly radiation damaged metamict zones "

Does this general statement refer to both grains. Are there recrystallized zones with bright CL in both grains. An unusual irregular patchwork of clear zircon can be seen around 3 the rim of grain B but no similar structure is evident in grain A. Has this structure been dated?

Some text has been added to make it clear that the fluid-assisted recrystallization texture is only present in Grain B. The rim on Grain B has not been dated due to high U content and highly radiation damaged structure. It also shows no magnetic features, which are confined to the centre of the grain. It is noted that the image of Grain B in the main CL figure is now a final remnant of the grain and has been polished in order to get the decent CL image. The resulting shallow angle has made the rim look larger than it really is, evident from the non-magnetic portion of the QDM image and the supplementary figure in which the polishing is explained.

Where are the strongly radiation-damaged metamict zones in the two grains? How is the degree of radiation damage determined? It has been shown that CL intensity decreases with radiation damage so zones in Grain A show a range of radiation damage. Some zones could be metamict.

In Grain A, more metamict zones are seen as a few fine layers within the oscillatory zoning, as clear in the images. These zones have a high porosity and complex damaged matrix, but were not a site of magnetite inclusions. In Grain B it is the rim, where the metamict zone is of interest in assisting fluids to the inner grain area. The text describes these regions in the main and Supplementary figures.

The mottled (CL) center of grain B could also be highly radiation damaged.

It is not. While it shows some level of alteration (the point of the paper) it is not metamict. This region still displays primary magmatic zoning, demonstrably different in both SEM-CL and the TEM images from the highly radiation damaged zones with more amorphous structure.

Line 85-86 . TEM lamellae were extracted from two grains (A and B?) within zones displaying primary oscillatory zoning (Fig.1a,e). The reviewer cannot see any primary oscillatory zoning in the part of grain B where the TEM lamellae was extracted (or anywhere else in the CL image of this grain on fig. 1e) (in the image received for reviewing).

As stated above this is covered in the Supplementary description of the Grain, and now made clearer in the main figure caption. The grain was polished after the TEM foil was extracted in order to get a better CL image displaying the primary zoning. The Supplementary image shows the TEM foil location in the original grain prior to that polish. The TEM foil itself is also clear evidence of this fact, showing ~2/3 primary igneous zoning.

What is a magnetite region? Is the “region” a broad shaped patch or what? Is it related to zone boundaries? Which parts of the grains have no magnetite inclusions

This is a typo and should say “magnetic region”, changed.

Lines 90-103. Microstructures in grain A

What are the dimensions of the dislocations. Are they essentially cracks? Could they be radiation damage expansion cracks?

The dimensions of the dislocation are evident from the image scale bars. They are atomic scale features with the dislocation cores of a diameter typically in the order of a few nanometers. These are demonstrably dislocations by any definition, composed of a high strain zone surrounding a core region of the dislocation. They are clearly distinct and on a different scale to the late expansion cracks seen in many zircon grains, or other macro-scale fractures seen here (see fractures in centre of Grain B TEM foil (Fig 1j)).

Line 98-101. Pores are frequently filled with precipitate phases such as magnetite , ilmenite and baddeleyite. How were these minerals identified? The implications of the presence of these secondary minerals on the conditions of formation of the secondary structures could be discussed.

This is a good point. Magnetite has clearly been identified as per the comment above. The others have been identified simply by STEM EDS chemical measurements. The ilmenite is highly unlikely to be anything else given the composition. However, the ZrO₂, which is clearly crystalline based on appearance of subtle Moire fringes and euhedral grain shapes, may not be true baddeleyite as we have no crystallographic information. We have altered the text and figures to simply say ZrO₂, and in the first instance stated that this *may* be baddeleyite.

For example the reviewer is of the view that the formation of baddeleyite from amorphous ZrO₂ would require quite a high temperature.

The high T requirement for this is not necessarily true. The article by Geisler (2007) states that ZrO₂ nanoparticles are a common feature of low T recrystallization of damaged zircon and in the presence of fluids at low T. In terms of the crystallinity state of ZrO₂, their morphology and the fact they are the most dense phase in the images (based on contrast) suggests it is not amorphous material.

Lines 105-114. The structural elements described here in general terms need to be supported by reference to relevant images. E.g. line 108 "we observe sinuous recrystallization fronts" and line 111 "preferred growth along intersecting dislocations" - needs a refer to relevant figure. As above it is recommended that more incisive descriptions (and figures) from the supplementary figures are transferred to the paper itself as supporting references for this discussion.

As stated above we have left the figure 2 and supplemental figure structure as is. But have made more clear references to the figures as suggested.

Line 109 . It is nor clear whether the metamict areas or the crystalline fronts contain defect rich crystalline zircon.

Text has been modified to clarify it is the recrystallized areas.

It would be interesting if further comment could be made on the origin of stacked dislocations and ring structures,(are they related to radiation damage expansion).

These structures are interesting but further description of them does not further the story. As with the smaller dislocation features, these are related to the space and defects

formed during volume expansion from radiation damage. The fluid recrystallization process seems to reorganise these structures into loops and lattices. Though without knowledge of the exact mechanisms and strains involved it would be speculative to comment further on their origin.

Is the “Moiré fringe structure ?” found in grains A and B and is it an exsolution texture? How is this used to determine that the secondary Fe phase is magnetite?

This is not exsolution feature, but an atomic/lattice scale observation. This is a specialist technique involving tilting of the TEM stage in order to create a crystal lattice interference pattern between the host and the inclusion. Given we know the host is zircon and the inclusion is Fe-oxide, there is a limit to the number of possibilities for the inclusion structure to produce the observed interference (d-spacing). In this case the 3 nm spacing means it can only be magnetite or possibly maghemite. This is explained in Supplementary Figure S11, and has now been made more clear in the text related to how magnetite was identified.

Line 127 A summary of the two mechanisms for the formation of secondary single-domain magnetite could be included here. Mechanism 1 fluid absent formation of dislocations providing pipe diffusion pathways for transport of Fe from external sources during radiation damage recovery, which suggests a whole grain process, and Mechanism 2 where defects bearing magnetite form in crystalline zircon as a result of fluid catalyzed recrystallisation fronts, suggesting a local generation of secondary magnetite. An issue here is that formation of the recrystallisation fronts may be much older than the radiation damage annealing.

This is not our interpretation, and also misses the difference between the two mechanisms. The fluid absent recovery process is ongoing, from when the zircon begins to accumulate damage and still continuing today. The fluid assisted process is more discrete, likely related to specific events within the rock unit. Our interpretation is the fluid assisted recrystallization is subsequent to the build-up of the fluid absent features, resulting in the reorganisation of microstructural features as described. While it is possible to fluid-alter pristine zircon, this is harder to do, and would not be exploiting the metamict zones (i.e., regions of accumulated damage) as clear ingress points. However, the relative timing (ignoring the continuous vs discrete argument) is not an issue. In either case to produce actual accommodation space for the magnetite, they are both significantly later than the zircon ages

Another issue is that both these processes may be much older than recent weathering that might be considered a source of the Fe.

Not an issue at all, again this is a key result of the paper. Both processes must be older than the Fe inclusions, as they are responsible for creating the space in which the Fe sits. The Fe being younger than the space accumulation resulting from radiation damage, and therefore significantly younger than the zircon is exactly what we are arguing for here.

Lines 163. Evaluation of the TEM images in this study shows a volume expansion of approximately 0.7%. Is this for the whole grain? How was this measured given the zircon

grains are inhomogeneous consisting of recrystallized parts (low expansion) and high U metamict parts (high expansion) all in the one grain?

As per the response to the first reviewer the text in this section has been modified. It is now made clearer that the 0.7% value is based on the observations of accumulated pore spaces within the zircon grain.

Line 164. Back calculated U and Th concentrations give 500-950Ma to produce the observed porosity. Does this imply a uniform U and Th content for the two grains, when it has been described elsewhere that the grains are heterogeneous in radiation damage and hence in U and Th.

No. The assumption is that the oscillatory zoning in CL is the result of trace element variation in elements such as U and, therefore, also matrix crystallinity. Variations on U and Th are therefore present at the scale of the zoning. However, this is too fine scale to be analysed individually. The laser ablation measurement of U and Th, therefore, is an average of the zones through which the TEM foil sits (as would be typical for a U–Pb analysis, for example). The fact that the microstructures and inclusions are not confined to any particular part of the zoning, but transect multiple zones of different actinide content means the average value is applicable to the scenario we describe.

Is the porosity uniform over the individual grains?

This is hard to say from the TEM images due to the small scale of the sample relative to the grain. It is possible that the higher U zones are slightly more porous, but not directly observed here. The key is that we are not looking at zones that have suffered extreme damage, and the level of porosity across the crystalline zones in question appear fairly uniform.

Line 166-168. The Fe source is the Jack Hills sediment itself, consistent with deep weathering and does not have a primary magmatic origin.

A weathering origin of the Fe has age implications (see comment on line 127) . Also, If the Fe is from low temperature weathering what are the implications of the presence of magnetite inclusions (and baddeleyite, ilmenite) on the conditions of incorporation of Fe into the zircons?

As with the reply to the earlier comment, the possibility of the source of Fe being sedimentary is one possibility offered by the estimate on the age of pore spaces. The text has been altered to make it clearer that fluid circulation within the precursor igneous rock OR a sedimentary origin for the Fe are possibilities afforded by the age estimate. However, the key point is that, in either case, it is significantly later than zircon crystallisation. In this manuscript, we are not making any definitive assertions as to the environmental conditions at the time of incorporation, as it is beyond the scope of these data to speculate. We accept the likely possibility that Fe could be incorporated over extremely protracted time periods and different conditions, rather than a single event, and that the age estimate is merely an upper bracket for magnetite formation.

Line 203. What does it mean that “ grains were initially surveyed for Pb isotopes using the Cameca ims 270”? If it means that the grains were isotopically analyzed with the Cameca

ims 270 the data should be included and the spot locations marked. This U and Th from the Cameca gives an important measure of the homogeneity of the grains, which can be compared with the results indicated in lines 227-228

This text has been reworded. A pre-screening session with rapid (low precision) acquisition times was run on the SIMS instrument in order to identify those grains with ancient Pb–Pb signatures. Following this, those grains with appropriately old ages (>3.5 Ga for this study) were analysed using a more typical set up for U–Pb analysis.

Line 227-228. U and Th measurements were made for the zircon grains alongside TEM locations in order to calculate radiation damage times.

What are radiation damage times and how are they calculated from the TEM data?

As per the earlier comment, the text has been altered to better describe the image analysis method used to determine the porosity associated with radiation damage. The reference given in the text (Murikami et al.) describes an experimentally calibrated method by which volume expansion of the crystal lattice can be linked directly to the ‘alpha dose’ received from the actinides within the grains. We have used the porosity as a proxy for volume expansion of the lattice to estimate our radiation damage times. As stated earlier, and covered in some detail in the Supplementary Figure S12, this is an estimate for many reasons. The important point is that the time frames suggested are in the region of 100’s of millions of years.

Where are the U and Th data?

It is recommended that i a table of analyses is included for comparison with the SIMS results and to show how the U and Th concentrations vary across the grains and how they relate to the zoning and the occurrence secondary structures.

The standard used for the SIMS analysis did not allow for U and Th concentrations to be calculated in the U–Pb sessions. Whilst it would be nice to look at U/Th variation across the grain, the area of importance is that of the TEM analysis from which the radiation damages were calculated. Due to the fact that a lot of additional work is planned for these grains, it was not permissible to use the destructive laser ablation technique to place multiple spots throughout the grain. The conversion of measured U and Th to the initial contents from the laser data is trivial, and the values quoted in the supplementary section are deemed appropriate detail for the manuscript.

We thank the reviewers once more for their comments, and look forward to hearing your decision in due course.

Kind regards

Dr. Rich Taylor